Journal of Molecular Liquids 460 (2026) 129935

Contents lists available at ScienceDirect

Journal of Molecular Liquids

journal homepage: www.elsevier.com/locate/molliq

Broadband THz time-domain spectroscopy of water: Enhanced cooperativity of hydrogen-bond dynamics in the Debye wing

A. Taschin [a, b,*], P. Bartolini [b], L. Caminiti [b, c,**], A. Boschetti [b, c], S. Fanetti [b, d], R. Torre [b, e]

[a] Consiglio Nazionale delle Ricerche – Istituto Nazionale di Ottica, CNR-INO, Via Nello Carrara 1, Sesto Fiorentino, 50019, FI, Italy
[b] European Laboratory for Non-Linear Spectroscopy (LENS), Università di Firenze, Via N. Carrara 1, Sesto Fiorentino, I-50019, Firenze, Italy
[c] Istituto Nazionale di Ricerca Metrologica, Strada delle Cacce 91, Torino, I-10135, Italy
[d] Consiglio Nazionale delle Ricerche – Istituto di Chimica dei Composti OrganoMetallici, CNR-ICCOM, Via Madonna del Piano 10, Sesto Fiorentino, I-50019, Firenze, Italy
[e] Dipartimento di Fisica e Astronomia, Università di Firenze, Via G. Sansone 1, Sesto Fiorentino, I-50019, Firenze, Italy

HIGHLIGHTS

- Broadband THz spectroscopy measurements on supercooled water.
- Debye wing is a clear signature of increasing cooperativity of the hydrogen-bond network dynamics.
- Debye wing cannot be directly associated with the structural α-relaxation of water.

ARTICLE INFO

Keywords:
Supercooled water
THz spectroscopy
Hydrogen-bonds
Debye-wing

ABSTRACT

Broadband terahertz time-domain spectroscopy measurements of liquid water are presented in the 0.3–12 THz frequency range from 360 K down to the supercooled regime at 255 K. The probed spectral window allows the characterization of the intermediate-frequency region linking the main Debye relaxation to intermolecular vibrational modes. The dielectric response is analysed using two alternative fitting schemes, yielding consistent fits despite the different parametrizations. Upon cooling, the dielectric response shows a progressive transfer of spectral weight from librational motions toward intermediate-frequency contributions demonstrating an enhancement of collective hydrogen-bond network dynamics. Comparison with depolarized Raman spectra reveals a separation between the fast dielectric components and the structural relaxation. The observed evolution is compatible with an increasing prevalence of tetrahedrally coordinated, LDL-like local environments. Our findings indicate that the apparent multiplicity of relaxation processes reflects a continuous spectrum of correlated hydrogen-bond network dynamics evolving toward increasingly cooperative behaviour upon cooling.

1. Introduction

The dielectric response of liquid water has been extensively investigated over several decades since the pioneering work of Debye [1]. Despite the large amount of theoretical, experimental and simulation work [2], its microscopic interpretation remains a subject of ongoing debate. The dielectric spectrum is dominated by a strong Debye relaxation with a peak in the GHz region, which explains water's exceptionally high static dielectric constant. Despite its apparently simple exponential form, this relaxation originates from a highly complex and heterogeneous hydrogen-bond (HB) network, whose dynamics extend over multiple spatial and temporal scales. Recent advances in high-frequency dielectric spectroscopy and broadband THz time-domain spectroscopy have extended experimental measurements over the 0.5–15 THz frequency range, bridging the gap between conventional dielectric spectroscopy and infrared spectroscopy [3–7]. These experiments have clearly revealed new features in the dielectric spectrum of liquid water; in

* Corresponding author at: Consiglio Nazionale delle Ricerche – Istituto Nazionale di Ottica, CNR-INO, Via Nello Carrara 1, Sesto Fiorentino, 50019, FI, Italy.
** Corresponding author at: European Laboratory for Non-Linear Spectroscopy (LENS), Università di Firenze, Via N. Carrara 1, Sesto Fiorentino, I-50019, Firenze, Italy.
Email addresses: andrea.taschin@cnr.it (A. Taschin), caminiti@lens.unifi.it (L. Caminiti).

https://doi.org/10.1016/j.molliq.2026.129935
Received 18 May 2026; Received in revised form 29 July 2026; Accepted 16 September 2026
Available online 18 September 2026

particular, a high–frequency "Debye wing" of the dielectric function extending from about 0.5 to 2 THz, where it merges into a spectral band centered around 4 THz. These findings demonstrate that the fast dynamical processes of liquid water, in addition to the well–known Debye relaxation, must be properly accounted for to explain the dielectric–THz spectrum [3–5,7–11].

Liquid water dynamics is an extremely complex process due to its intrinsically collective nature, governed by the molecular hydrogen-bond (HB) network. This complexity is clearly reflected in the dielectric spectrum of water, and previous studies have employed a wide variety of models to reproduce the experimental observations. In the following, we summarize the main approaches.

A large number of studies have adopted a phenomenological description of the dielectric spectrum. According to these *phenomenological models* the spectrum is represented as a sum of independent spectral functions, each tentatively associated a posteriori with a specific dynamical process of liquid water. In some of these studies [4,7–9,12], the dielectric spectrum is described as a sum of ad hoc Debye relaxations; one or two additional Debye terms are typically required to reproduce the spectral wing. Moreover, vibrational contributions are often included alongside the relaxation processes to account for the spectrum at higher frequencies [4,5,13]. However, such decompositions are not unique and frequently lead to inconsistent parameter values and temperature trends across different studies. This ambiguity reflects the intrinsic difficulty of representing a continuous spectrum of relaxation processes with a discrete set of separated contributions. In particular, it has been shown that fitting the high-frequency excess with additional Debye terms can be problematic and model-dependent [2].

More recently, a series of *dynamic models* has been introduced, in which the dielectric spectrum is computed directly from a specific water model. These approaches aim to identify, within the complex dynamics of water, the key processes that determine its dielectric response. In this context, Popov and coworkers [11] proposed that the primary Debye relaxation originates from the migration of defects within the HB network, while deviations from ideal Debye behavior at high frequencies arise from collective fluctuations of the same network. Similarly Gaiduk and co-workers [14,15] suggested that this faster dynamic response is associated with vibrational dynamics of hydrogen bonds, involving coupled bending and stretching motions rather than nearly free molecular rotations. Within this framework, the Debye wing, more generally the dielectric spectrum lying at relatively high frequencies, appears as the high-frequency manifestation of HB network dynamics that give rise to the primary Debye relaxation. Alternative approaches based on semi-microscopic models have also been proposed to describe the dielectric response of water over a broad frequency range. In particular, models developed by Artemov, Volkov and coworkers [16,17] interpret the dielectric spectrum in terms of coupled diffusive and oscillatory motions, often involving charge transport and proton dynamics. In these frameworks, the Debye relaxation and the higher-frequency response are described as manifestations of distinct processes related to molecular diffusion and ion dynamics.

In our opinion, many of the phenomenological models give an oversimplified interpretation of the spectral functions by associating them directly with uncoupled water dynamic processes. Nevertheless, despite the evident difficulties of phenomenological descriptions in extracting unique spectral parameters and in unambiguously linking them to water dynamics, they remain a very useful approach to experimental data, providing a first valuable insight into the properties of water. Dynamic models certainly represent a step forward compared to phenomenological models in the interpretation of the dielectric spectrum, as collective and coupling effects can be explicitly taken into account. However, given the intrinsic complexity of water dynamics, the underlying physical models often fail to adequately reproduce the collective molecular phenomena present in liquid water.

Moreover, a significant limitation of both phenomenological and dynamic models is the lack of a convincing comparison with more recent physical models of liquid water dynamics [18–22]. Within this broader framework, liquid and supercooled water have often been interpreted in terms of the coexistence of distinct local structural environments, commonly referred to as high-density liquid (HDL) and low-density liquid (LDL) [18–21]. These local configurations extend over nanoscopic lengths [23,24] and dynamically interconvert on very fast timescales [22,25] and are characterized by different degrees of tetrahedral organization of the hydrogen-bond network, as well as different levels of intermolecular cooperativity. Such a picture should be taken into account when describing the distribution of relaxation processes observed in the dielectric response.

From the experimental point of view, a major limitation of many previous studies is the restricted spectral window and limited signal-to-noise ratio, which can bias the fitting procedure and lead to ambiguous interpretations of the intermediate frequency response. The apparent intensity and temperature dependence of secondary Debye processes are in fact highly sensitive to the accessible frequency range and to the specific fitting model adopted. Extending the characterization of the dielectric function to higher frequencies, up to a few THz, and including intermolecular modes in the far-infrared with a better signal-to-noise ratio, would allow for a more accurate assessment of this weak dynamic contribution, which is partly masked by the dominant Debye relaxation.

In this work, we report measurements of the absorption coefficient and refractive index of water as a function of temperature, down to the supercooled temperature of 255 K, over a broad frequency range, of 0.3–12 THz. To widen the measured spectral window, we performed measurements using two complementary THz-Time Domain Spectroscopy (TDS) setups. One used two photoconductive antennas (PCAs) for THz generation and detection [26], covering the spectral range 0.3–3.5 THz, and another used THz plasma generation and Air-Biased Coherent Detection (ABCD) [27,28], which allowed us to cover the 0.5–12 THz frequency range. Data were collected in transmission configuration, on a water sample with a thickness of only 27 μm, and in an ATR configuration. The dielectric response of water was systematically compared with numerical evaluations obtained using different fitting models. We demonstrate that the dielectric response undergoes a continuous evolution from more local molecular dynamics at high temperature to increasingly collective behaviour upon cooling. This trend is consistently observed with two different phenomenological fitting models, indicating that it reflects an intrinsic property of the hydrogen-bond network rather than a model-dependent artifact. This interpretation is also supported by recent simulations [29,30] in which the cooperative character of the THz part of the spectrum is clearly shown. Within this framework, the observed increase of cooperativity upon cooling is consistent with a progressively larger contribution of LDL-like local structures, characterized by a more tetrahedral hydrogen-bond network and enhanced dynamical correlations.

Finally, by comparing the dielectric loss with the depolarized Raman susceptibility [22,31] at low temperatures in the supercooling region, we are able to identify the different frequency windows in which the fast relaxation and structural relaxation processes of water take place. The distinct temperature–dependent evolution observed suggests that the Debye wing is not directly identifiable with the α-structural relaxation and it may arise from different microscopic mechanisms.

Ultimately, the need to introduce additional relaxation processes should be interpreted as the manifestation of a continuous spectrum of correlated hydrogen-bond network dynamics, rather than as evidence for distinct independent molecular relaxations. This interpretation reconciles apparently conflicting results reported in the literature and highlights the crucial role of broadband measurements in capturing the intrinsically multi-scale and cooperative nature of water dynamics.

2. Experimental aspects

To cover a broader spectral range, we combined two THz-TDS setups based on different generation and detection schemes (further

experimental details are provided in the Supplemental Material (SM)). The low-frequency region (0.3–3.5 THz) was measured using a standard THz-TDS configuration [26], where THz pulses are generated and detected via optical excitation of low-temperature GaAs PCAs by an Er-doped fiber femtosecond laser. The high-frequency portion of the spectrum (up to 12 THz) was measured using a broadband THz-TDS setup based on two-colour laser-induced air plasma generation combined with Air-Biased Coherent Detection (ABCD) [27,28]. In this configuration, intense femtosecond pulses from a Ti:sapphire Chirped Pulse Amplification system are focused in air to generate a plasma filament by mixing the fundamental and second harmonic fields. The resulting nonlinear interactions produce ultra-broadband THz radiation with a spectral bandwidth comparable to the optical pulse bandwidth. Detection of the THz electric field is achieved through the ABCD technique, in which the THz pulse and a synchronized optical probe pulse are collinearly focused in air, generating a second-harmonic signal via the third-order nonlinear response of the gas. The THz electric field is retrieved in both experiments through heterodyne detection. THz-TDS experiments provide simultaneous measurements of both the amplitude and phase of the THz transient electric field over a very broad spectral range. All THz beam paths, in both setups, were enclosed in a nitrogen-purged chamber in order to minimize absorption by atmospheric water vapour.

Transmission measurements were performed using a home-built liquid cell consisting of two diamond windows separated by a 27 μm spacer defining the optical path length. The cell was temperature controlled by a closed-cycle helium cryostat with stability of ±0.1 K, allowing measurements down to the supercooled region (255–360 K). The small optical path length is required due to the strong absorption of water in the THz range, which would otherwise severely attenuate the transmitted field [6,32].

ATR measurements were performed using a 45° silicon prism mounted in a custom-made Teflon cell with separate sample and reference compartments. Temperature control was achieved using a thermoelectric liquid chiller with stability of ±0.1 K, enabling measurements in the range 279–365 K. It was not possible to take measurements in the supercooling region in the ATR geometry, since water rapidly crystallized below the melting point.

The standard THz-TDS setup based on PCAs was mainly used in ATR configuration, while the broadband air-plasma setup was primarily employed in transmission geometry. The combination of transmission and ATR measurements enables reliable determination of the dielectric function over a broad spectral range and a wide temperature interval.

In both experimental setups, the sample cells are placed on a motorized translation stage to allow insertion into and extraction from the THz path. A reference measurement is taken for each single sample measurement. This reduces the effects of signal differences between reference and sample that can occur on very slow timescales, such as those due to temperature fluctuations, which are not related to the sample's optical properties (more details about THz-TDS data are reported in the SM).

To extract the optical parameters of water from the acquired transmission THz data, we performed a complex analysis, which compares the experimental transfer function with the theoretical transfer function of the sample cell. This is considerably more complex than the transfer function of a single-layer sample because it has to take into account the three-layer window-water-window system. Our transfer function must include, in addition to the propagators in the individual layers and the reflection and transmission coefficients through the various layers, also all the Fabry-Perot terms arising from the multiple reflections between the involved surfaces. To build the transfer function we follow the derivation reported in [33] where Fabry-Perot terms are considered with an infinite number of reflections. The analysis for the optical parameter extraction is similar to that used and reported in our previous paper [26] for two-layer samples. The analysis relies on an accurate knowledge of the optical parameters and thickness of the diamond windows, which have been, therefore, previously measured by performing the THz-TDS experiment on the diamond windows alone.

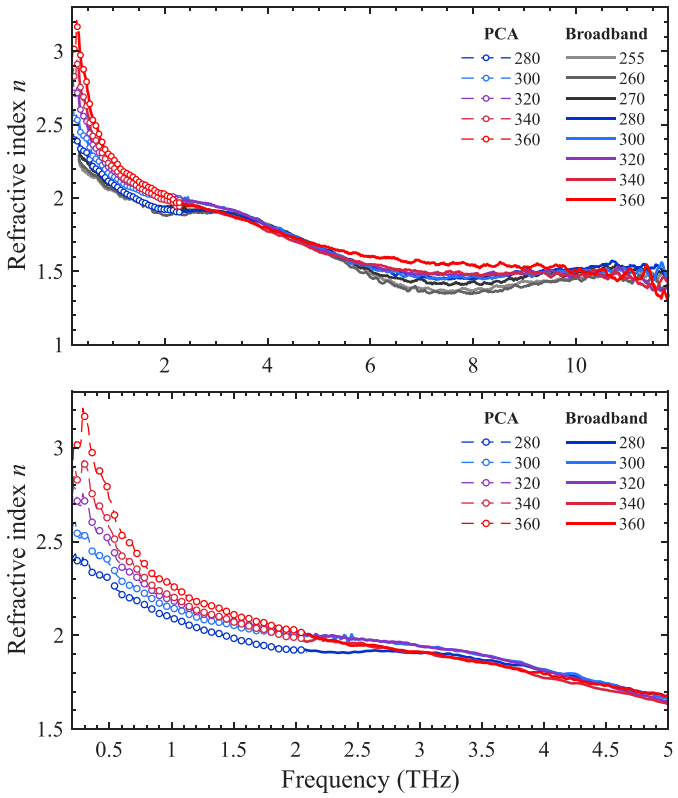

Fig. 1. Frequency dependence of refractive index of water as a function of temperature measured with broadband THz-TDS setup in transmission configuration and with the PCA THz-TDS setup in ATR configuration. The agreement between the data obtained with the two different THz-TDS setups is very good extending the probed spectral range from almost 0.3 to 12 THz. The lower panel shows a magnified view of the low-frequency region. For visual clarity, only a subset of PCA markers is displayed.

Measurements on water in ATR configuration, with both the THz-TDS setups, were carried out using the silicon prism cell previously described. For optical parameter extraction we used the calibration and analysis procedure reported in [34].

In Figs. 1 and 2, we show the frequency behaviour of refractive index and absorption coefficient of water as a function of temperature measured with broadband THz-TDS setup in transmission configuration and with the PCA THz-TDS setup in ATR configuration. In these figures, we omit the data in the overlapping frequency range to avoid overcrowding; these data are instead reported in Fig. S7 in SM for room temperature. The quality of the measured values is excellent, and the agreement between the data obtained using the two different THz-TDS configurations is outstanding, with a spectral analysis range spanning approximately 0.3 to 12 THz.

3. Data analysis and discussion

As a check of the reliability of the optical parameters extracted from the broadband transmission measurements, we also made a measurement in ATR configuration with the broadband THz-TDS setup at room temperature. ATR measurements, even if in our case noiser than those in transmission mode (see Fig.S7 of SM), do not suffer from uncertainties related to the sample thickness or Gouy shift [35–38] errors and generally provide more reliable values of the refractive index and absorption coefficient. Comparison between the optical parameters obtained by the broadband THz-TDS setup with the two configurations, transmission and

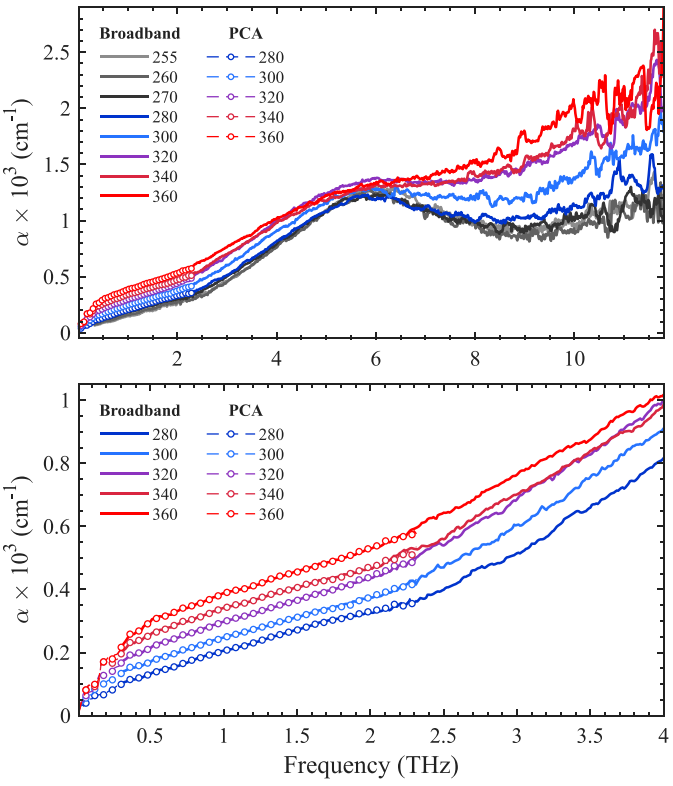

Fig. 2. Frequency dependence of the absorption coefficient of water as a function of temperature measured with broadband THz-TDS setup in transmission configuration and with the PCA THz-TDS setup in ATR configuration. The agreement between the data obtained with the two different THz-TDS setups is very good extending the probed spectral range from almost 0.3 to 12 THz. The lower panel shows a magnified view of the low-frequency region. For visual clarity, only a subset of PCA markers is displayed.

ATR, and the most important data reported in the literature at room temperature is shown in Fig.S7 of SM. Some of the literature data were obtained by Fourier-Transform Infra-Red (FTIR) spectroscopy measurements in ATR, reflection or transmission configuration. It is worth noting that in these measurements the values of the refractive index are not directly measured but calculated from the values of the absorption coefficient through the Kramers-Kronig relations and this procedure relies on the complete knowledge of $\alpha(\omega)$ at all the frequencies. We would like to emphasize the importance of performing THz-TDS measurements for the simultaneous measurement of optical parameters. Furthermore, other literature data are obtained by THz-TDS setups in ATR or reflection configuration only in a narrow THz range (0.1–2 THz). Only one paper reports measurements in transmission configuration, on a free-standing film of water, with a broadband THz-TDS setup similar to ours [6].

From the experimental values of n and α we can calculate the real and imaginary parts of the dielectric constant of water and compare them with the models usually employed to describe the frequency evolution of the dielectric constant. THz-TDS spectroscopy, like dielectric spectroscopy and infrared absorption spectroscopy, is sensitive to collective dynamics and it is directly connected to the complex dielectric constant, $\varepsilon(\omega)$. This response function can be expressed, in the linear response approximation, as a correlation function of equilibrium properties [39,40]:

$$\frac{\tilde{\varepsilon}(\omega)-1}{\varepsilon_S-1}=\int_0^\infty e^{i\omega t}\left[-\frac{d\Phi(t)}{dt}\right]dt \tag{1}$$

where

$$\Phi(t)=\frac{\langle \mathbf{M}(t)\cdot\mathbf{M}(0)\rangle}{\langle \mathbf{M}(0)\cdot\mathbf{M}(0)\rangle}, \tag{2}$$

$\mathbf{M}(t)$ is the total dipole moment of the system defined as [39]:

$$\mathbf{M}(t)=\sum_j \mathbf{m}^j(t) \tag{3}$$

with $\mathbf{m}^j$ the effective molecular dipole moment containing the permanent molecular dipole moment and the induced dipole moment.

Usually, for water the correlation function appearing in Eq. (1) has been described as a sum of exponential relaxations and damped harmonic oscillators [3–5,9,13,41,42] with a variable number of contributions depending on the explored time relaxation window or frequency range. In particular, translated into the frequency domain in the GHz-THz range, water shows a main relaxation absorption peak around 20 GHz, well reproduced by a Debye relaxation [1], a second fast Debye relaxation, and sometimes a third one, necessary for reproducing the high-frequency excess wing around 1 THz not well reproduced by the first Debye mode, and two vibrational contributions at 5 THz and 15 THz ascribed to the intermolecular stretching and librational modes respectively. The intermolecular bending mode at around 2 THz (60 cm^{-1}) clearly visible in the depolarized Raman spectroscopy [22,31] is strongly hindered. In some literature on dielectric spectroscopy this mode has been considered although with very weak weight [2,5]. In his review article [2], Elton shows that describing the THz excess of the dielectric response of water by introducing multiple additional relaxation terms beyond the main Debye process and the intermolecular vibrational modes is often redundant and not uniquely justified. In particular, he emphasizes that modelling such a complex relaxation spectrum, in which diffusional and vibrational dynamics continuously merge due to the heterogeneous nature of the hydrogen-bond network, is mathematically ill-posed when represented as a discrete sum of independent processes. Molecular dynamics simulations have shown that this frequency window (≈20–200 cm^{-1}) is dominated by collective intermolecular modes involving correlated motions of several molecules within the hydrogen-bond network. In particular, Heyden et al. [29] demonstrated that the THz spectrum arises from spatial correlations extending over multiple hydration shells, while more recent simulations by Sharma et al. [30] have shown that the spectral features in this region originate from the interplay between permanent and induced dipole correlations acting over different length scales. These results support the view that the Debye wing reflects cooperative hydrogen-bond network dynamics rather than a superposition of independent molecular relaxations.

We fit the measured complex dielectric response using two alternative models: (Model 1) two Debye relaxations plus two damped harmonic oscillator (DHO) contributions, and (Model 2) one Debye relaxation plus three DHOs:

$$\varepsilon(\omega)=\sum_{i=1}^{2}\frac{\Delta\varepsilon_i}{1+i\omega\tau_i}+\sum_{j=1}^{2}\frac{A_j\,\omega_j^2}{\omega_j^2-\omega^2+i\omega\gamma_j}+\varepsilon_\infty, \tag{4}$$

$$\varepsilon(\omega)=\frac{\Delta\varepsilon_1}{1+i\omega\tau_1}+\sum_{j=1}^{3}\frac{A_j\,\omega_j^2}{\omega_j^2-\omega^2+i\omega\gamma_j}+\varepsilon_\infty, \tag{5}$$

here, $\Delta\varepsilon_i$ and τ_i are the amplitudes and relaxation times of the Debye processes, while A_j, ω_j, and γ_j are the amplitudes, resonance frequencies, and damping constants of the DHO contributions. Depending on the selected model, these terms account for the slow Debye relaxation, a possible fast Debye relaxation, the intermolecular stretching and librational modes, and the *bending–umbrella* mode [29], which is included when a third DHO replaces the second Debye term, as in the second model. In what follows, we will use the subscripts S, L, and B–U for the parameters of these three DHOs. Finally, ε_∞ is an effective high-frequency dielectric constant, approximately equal to the square of the

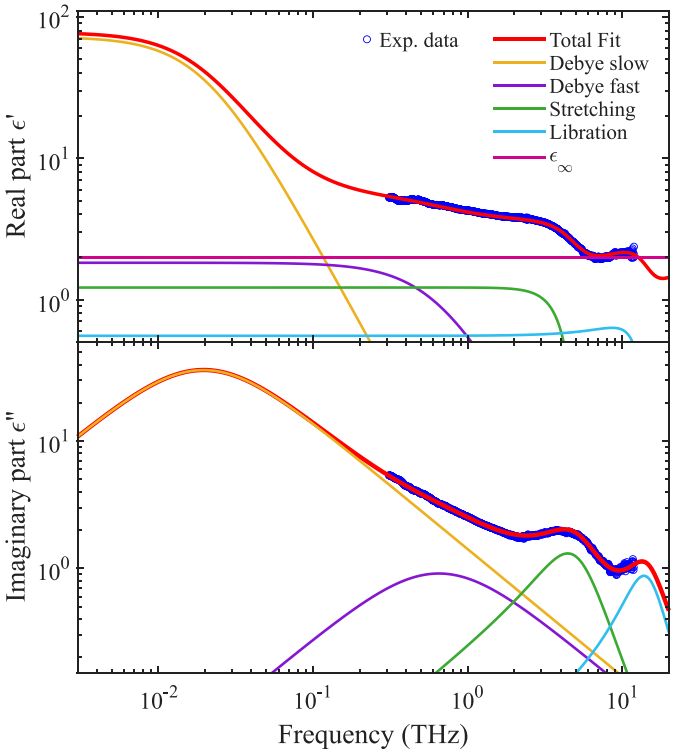

Fig. 3. Frequency behavior of real (upper) and imaginary (lower) parts of the complex dielectric constant of water at 300 K obtained from experimental values of n and α along with the fitting results obtained using the model 1. The individual contributions are also shown: slow first Debye relaxation (dark yellow), second Debye relaxation (purple), stretching DHO mode (green), librational DHO mode (cyan), and ϵ_∞ (magenta).

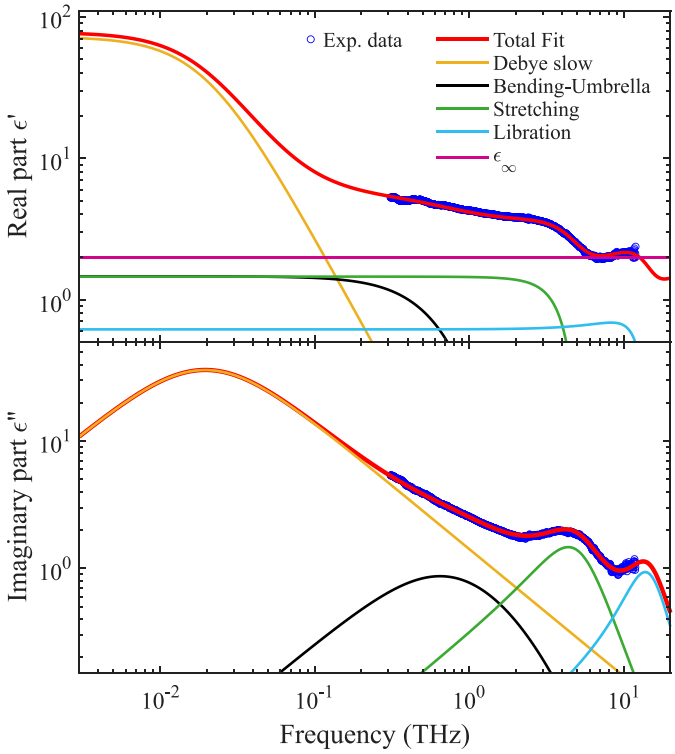

Fig. 4. Frequency behavior of real (upper) and imaginary (lower) parts of the complex dielectric constant of water at 300 K obtained from experimental values of n and α along with the fitting results obtained using the model 2. The individual contributions are also shown: slow first Debye relaxation (dark yellow), bending–umbrella DHO (black), stretching DHO mode (green), librational DHO mode (cyan), and ϵ_∞ (magenta).

refractive index at optical frequencies ($\epsilon_\infty = n_{vis}^2$), which has been kept fixed at the value of 1.78 in all the fits.[1]

Within the frequency window covered by our measurements, the data do not allow a reliable determination of the slow relaxation time and the librational mode frequency. These parameters were therefore fixed to the literature values. In particular, τ_1 was obtained from the interpolation and extrapolation of the values tabulated in [7], while the librational frequency was taken from [4]. The remaining model parameters were allowed to vary freely during the fitting procedure. Finally, considering that in the limit $\omega \to 0$ Eqs. (4) and (5) become:

$$\varepsilon_S = \sum_{i=1}^{2} \Delta\varepsilon_i + \sum_{j=1}^{2} A_j + \varepsilon_\infty, \tag{6}$$

and

$$\varepsilon_S = \Delta\varepsilon_1 + \sum_{j=1}^{3} A_j + \varepsilon_\infty, \tag{7}$$

with ε_S being the static dielectric constant. We constrained all amplitudes to satisfy the above relations by fixing ε_S using the empirical expression adopted in Ref. [4]. This expression is consistent with available static-permittivity data over the investigated temperature range including direct low-frequency measurements in the stable liquid [43], and the critically evaluated supercooled-water data compiled in Ref. [44]. The amplitudes were constrained using a normalized-weight parametrization based on the softmax transformation [45], as described in detail in the SM. This procedure enforces the static-limit condition, $\sum_k S_k = \varepsilon_S - \varepsilon_\infty$, where S_k denotes the dielectric strength of each active Debye or DHO contribution, while keeping the relative spectral weights of the active components adjustable and preventing unphysical negative amplitudes. The values adopted for τ_1, ω_L, and ε_S as a function of temperature, together with the full set of fitted parameters obtained from both models, are reported in the SM. For both fitting models, the intermolecular stretching mode exhibits the expected blue shift upon cooling, while the damping constants of both the stretching and librational modes decrease monotonically with decreasing temperature (see Figure S9 in the SM), indicating a physically consistent temperature evolution of the fitted DHO parameters.

In Figs. 3 and 4 we report, on a log–log scale, the experimental data for the real (upper panel) and imaginary (lower panel) parts of the dielectric function together with the corresponding fits obtained from Eqs. (4) and (5) at T = 300 K. The frequency range has been extended beyond the experimentally accessible window in order to better highlight the relative contributions of the different fitting components. Both models reproduce the experimental spectra with comparable accuracy, yielding nearly indistinguishable fits over the entire investigated frequency range. This result indicates that the experimental data do not allow for a clear distinction between a representation based on one Debye term plus three DHO terms and one based on two Debye terms plus two DHO terms. As Elton has already pointed out in his in-depth analysis [2], the excess dielectric response at THz frequencies can be described equivalently by different functional decompositions, reflecting the inherent difficulty of representing a broad and continuous

[1] ϵ_∞ should not be confused with $\epsilon(\infty)$, which is the response at infinite frequency. In any physical system $\epsilon(\infty) = 1$, ϵ_∞ is instead the response arising from electronic resonances when we measure well below them, its value may be different depending on the probed frequency window and the employed fitting model.

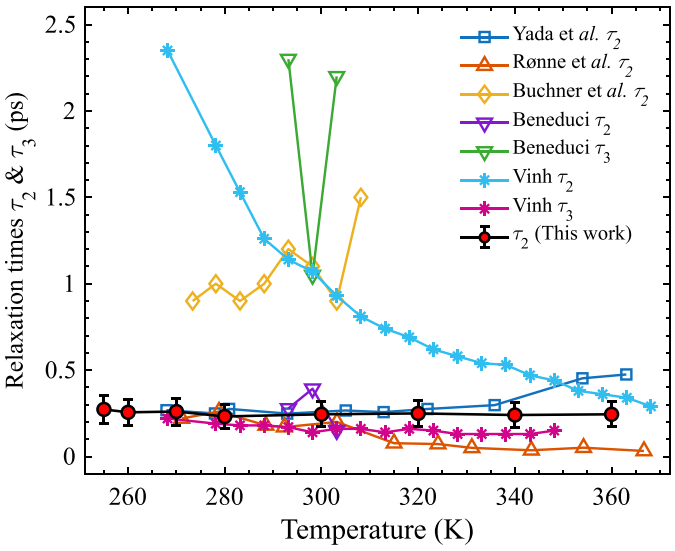

Fig. 5. Temperature behaviour of the relaxation times of the fast Debye component extracted from the fitting analysis based on model 1 is compared with the literature values: Yada et al. [4], Rønne et al. [3], and Buchner et al. [9], who use two Debye terms; Beneduci [10] and Vinh et al. [7], who use three Debye terms.

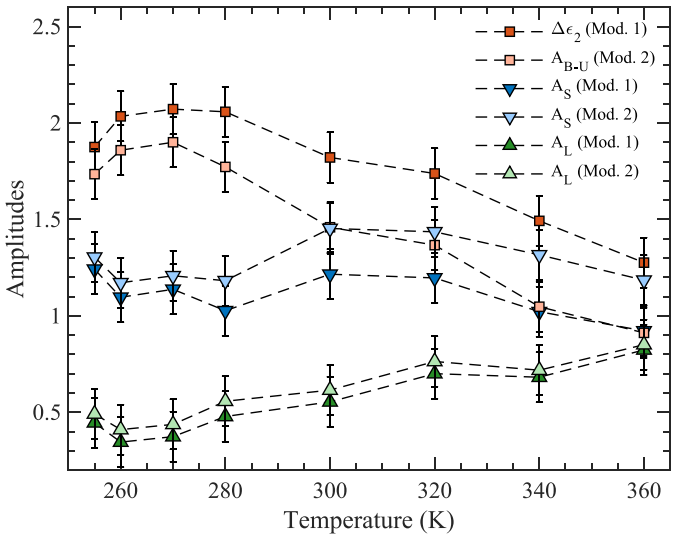

Fig. 6. Temperature dependence of the amplitudes associated with the different modes for both fitting models. The progressive increase in the intermediate-frequency component ($\Delta\epsilon_2$ for model 1 and A_{B-U} for model 2), with decreasing temperature, and the simultaneous decrease of the librational amplitude (A_L) indicate a redistribution of spectral weight toward more collective and cooperative intermolecular dynamics upon cooling. (solid symbols: model 1, lighter symbols: model 2.)

distribution of relaxation processes with a limited number of discrete terms.

As a first step, we analyse the temperature dependence of the relaxation time associated with the fast Debye process obtained from the fit using the first model (Mod.1), see Eq. (4). The resulting values of τ_2 are shown in Fig. 5, together with literature results obtained using the same formalism and alternative parametrizations including three Debye contributions. Specifically, we compare our results with those reported by Yada et al. [4], Rønne et al. [3], and Buchner et al. [9], who use two Debye terms, as well as with Beneduci [10] and Vinh et al. [7], who use three Debye terms. What immediately emerges is the wide spread of values reported in the literature for τ_2 and τ_3. This variability arises both from the different functional forms used to describe the Debye wing contribution and from the different spectral windows explored in the various studies. This observation further confirms that these dynamics cannot be simply represented as the sum of independent additional relaxation processes. Instead, it highlights the importance of measuring over a sufficiently broad spectral range and with a very high signal-to-noise ratio in order to properly resolve the weak intermediate-frequency dynamics, which are partially masked by the dominant Debye relaxation. Interestingly, our results show that the relaxation time associated with the fast Debye process, τ_2, remains nearly constant over the investigated temperature range. This behaviour indicates that the fast component cannot be interpreted as an independent diffusive relaxation that progressively slows down upon cooling, as observed for the main Debye process. Rather than representing a distinct molecular relaxation with its own temperature-dependent time scale, this contribution likely provides an effective description of a broader distribution of intermolecular dynamics of the hydrogen-bond network.

In this framework, the marked increase in the corresponding amplitude $\Delta\epsilon_2$ (see Fig. 6) upon cooling suggests that this spectral component becomes progressively more relevant at lower temperatures. Furthermore, the simultaneous decrease in the amplitude of the librational mode, typically associated with the less tetrahedral high-density liquid (HDL) form of water, suggests that upon cooling the balance progressively shifts toward the low-density liquid (LDL) fraction. Within this interpretation, LDL-like local environments would correspond to a more extended hydrogen-bond network and a higher degree of cooperativity among the different dynamical contributions. Consistently, the amplitude of the intermolecular stretching mode shows only a weak temperature dependence. Distance-resolved molecular simulations indicate that the intermolecular stretching band is dominated by hydrogen bond dynamics within the first solvation shell, although contributions from longer range dipolar correlations are not excluded [29,30]. Within the present single DHO representation, this broad contribution may contain unresolved dynamics associated with different local hydrogen bond environments. Its total spectral weight is therefore not expected to scale directly with the relative populations of HDL- and LDL-like configurations. Instead, cooling mainly affects the dynamical parameters of the stretching contribution, as reflected by the progressive blue shift of its resonance and the reduction of its damping, consistent with increasing hydrogen-bond stiffness and a narrower distribution of local dynamics. The almost temperature independent stretching amplitude therefore indicates that the dominant spectral-weight redistribution observed in our fits occurs between the librational and intermediate frequency contributions, rather than through a substantial change in the total stretching spectral weight.

As a second step in our analysis, we fitted the data using the second model (Mod.2); see Eq. (5). As noted earlier, the quality of the fit is comparable to the previous one. When we replace the second Debye term with a DHO, which we identify as the bending–umbrella mode, a very interesting feature emerges. In contrast to the parameters associated with the other DHO contributions, which exhibit the expected temperature evolution (see Figure S9 of the SM), this third DHO shows a transition from critical damping to an increasingly overdamped character as the temperature decreases (see Fig. 7). This behavior suggests the emergence of an enhanced cooperative character in the THz intermediate dynamics upon cooling. The transition from a critical to an overdamped regime indicates that the oscillation of the bending–umbrella mode becomes heavily coupled with the surrounding environment. As reported for the previous model, this reflects the progressive strengthening and increasing correlation of H-bonds within the network. Once again, this is compatible with a scenario where, upon cooling, the balance between HDL and LDL forms progressively shifts toward the LDL fraction. This scenario is further supported by the temperature-dependent trends of the amplitudes for both the bending–umbrella and librational modes

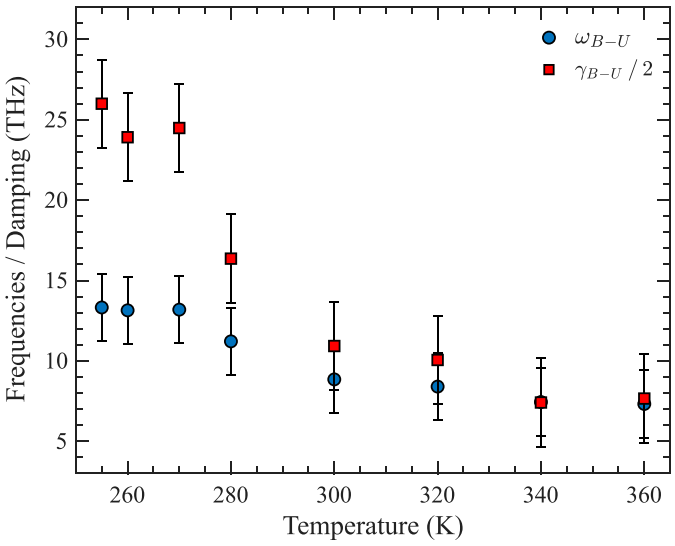

Fig. 7. Temperature dependence of the frequency ω_{B-U} and half the of damping constant $\gamma_{B-U}/2$ for the bending-umbrella DHO mode. As the temperature decreases, the damping constant increases relative to the frequency; this DHO exhibits critical damping at high temperatures, becoming increasingly overdamped as the temperature decreases. This behaviour highlights the emergence of an increasingly cooperative nature in the system's intermediate THz dynamics.

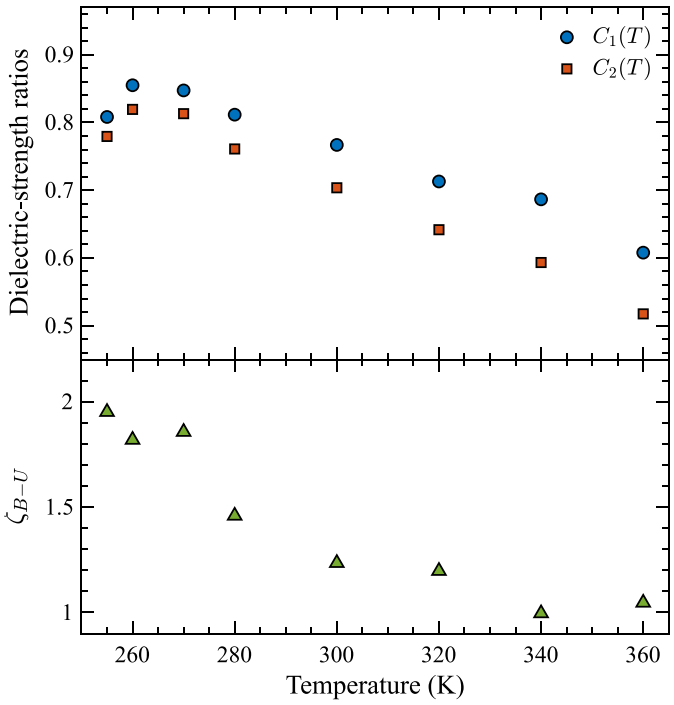

Fig. 8. Temperature dependence of the normalized dielectric-strength ratios $C_1(T)$ and $C_2(T)$ obtained from Eqs. (8) and (9), respectively (upper panel). These quantities describe the relative dielectric strength of the intermediate-frequency contribution with respect to the sum of the intermediate-frequency and librational contributions. The lower panel shows the damping ratio of the bending–umbrella contribution, as defined in Eq. (10). The increase of both $C_1(T)$ and $C_2(T)$ upon cooling, together with the increasing $\zeta_{B-U}(T)$, indicates a redistribution of dielectric strength toward the intermediate-frequency dynamics accompanied by an increasingly overdamped response.

(see Fig. 6). The redistribution of spectral weight between these contributions suggests a structural reorganization of the H-bond network, consistent with the progressive dominance of the LDL-like environment at lower temperatures.

To quantify the redistribution of dielectric strength between the intermediate-frequency and librational contributions, we introduce the normalized ratios

$$C_1(T) = \frac{\Delta\varepsilon_2(T)}{\Delta\varepsilon_2(T) + A_L(T)}, \tag{8}$$

for Model 1, and

$$C_2(T) = \frac{A_{B-U}(T)}{A_{B-U}(T) + A_L(T)}, \tag{9}$$

for Model 2. In the present parametrization, $\Delta\varepsilon_2$, A_{B-U}, and A_L represent contributions to the static dielectric constant and are therefore proportional, through the zero-frequency Kramers–Kronig relation, to the corresponding dielectric-loss spectra integrated over logarithmic frequency [46]. These ratios quantify the redistribution of dielectric strength and should not be interpreted as microscopic structural fractions or direct measures of cooperativity. The dynamical character of the bending–umbrella contribution is examined separately through its damping ratio,

$$\zeta_{B-U}(T) = \frac{\gamma_{B-U}(T)}{2\omega_{B-U}(T)}. \tag{10}$$

Fig. 8 shows the temperature dependence of the normalized dielectric-strength ratios $C_1(T)$ and $C_2(T)$ in the upper panel, while in the lower panel it reports the corresponding evolution of the damping ratio $\zeta_{B-U}(T)$.

As shown in Fig. 8, both $C_1(T)$ and $C_2(T)$ exhibit a marked overall increase upon cooling. Despite the different parametrizations of the dielectric response, the two definitions show similar temperature dependences. A sensitivity analysis, performed by systematically varying the fixed parameters ε_S and τ_1 within their estimated uncertainties, shows that these variations moderately affect the absolute values of $C_1(T)$ and $C_2(T)$ without altering their overall increase upon cooling. In particular, the enhanced relative dielectric strength of the intermediate-frequency contribution in the low-temperature region remains robust under all tested variations (see Fig. S10 of the SM). These results indicate that the progressive enhancement of hydrogen-bond-network cooperativity represents a robust physical feature rather than a model-dependent artifact.

Within structural scenarios describing water in terms of a continuous distribution of local environments with different degrees of tetrahedral order, this behavior is qualitatively consistent with the commonly observed increase of tetrahedral configurations at lower temperature [47]. These local configurations should not be regarded as static structural species, but rather as dynamically evolving arrangements continuously reshaped through hydrogen-bond rearrangements. The progressive increase of the intermediate-frequency spectral weight, together with the crossover of the bending–umbrella mode from near critical to overdamped behavior, indicates that the Debye wing reflects the increasing cooperativity of intermolecular motions within a dynamically evolving hydrogen-bond network. Within this framework, the enhanced prevalence of LDL-like local configurations upon cooling does not imply the emergence of distinct molecular species, but rather a gradual shift in the balance between local environments characterized by different degrees of tetrahedral order.

We also tested the theoretical framework proposed by Popov et al. [11], in which dielectric relaxation originates from the migration of orientational defects within the hydrogen-bond network. When applied to the present dataset, and combined with broadband spectra from Vinh et al. [7], the Popov relaxation function systematically converges to the Debye limit, thereby preventing a reliable separation of the two intrinsic time scales predicted by the model. In this situation, the additional intermolecular contribution is effectively accounted for by

the same DHO component identified within the simpler phenomenological models. This result does not imply a failure of the Popov model, which provides a physically appealing microscopic description of dielectric relaxation in terms of defect-mediated hydrogen-bond network dynamics. Rather, it suggests that the spectral signature associated with the predicted distribution of relaxation times is extremely weak and requires an even broader spectral window and an improved signal-to-noise ratio in the THz region in order to be unambiguously resolved.

For completeness, we also considered the stochastic frequency modulation (SFM) approach proposed by Shiraga et al. [5], in which both the main Debye and fast relaxation are described in terms of overdamped vibrational dynamics rather than Debye-like relaxations. The authors introduced this model to address the issue that Debye responses contribute in a non-physical way to the dielectric response at high frequencies. Within this framework, the intermediate contribution is intrinsically represented in an overdamped regime at all the temperatures and therefore does not explicitly display the critical-to-overdamped crossover observed when the bending–umbrella mode is treated as a pure DHO. Nevertheless, the temperature evolution of the spectral weight remains consistent with the behaviour obtained from the phenomenological models discussed above. This comparison further supports the conclusion that the observed increase of cooperativity reflects an intrinsic property of the hydrogen-bond network dynamics rather than a consequence of the specific parametrization adopted.

To further clarify the physical nature of these intermediate dynamics, we compare the dielectric response with depolarized Raman susceptibility measurements in the supercooled region. In Fig. 9 we report the third–order susceptibility at 253 K obtained from the imaginary part of the Fourier transform of the optical Kerr effect signal measured in our previous works [22,31], together with the imaginary part of the complex dielectric response at 255 K. The structural relaxation observed in the Raman susceptibility exhibits a strong temperature dependence and shifts rapidly toward lower frequencies upon cooling, while the characteristic time associated with the intermediate dynamics remains comparatively weakly temperature dependent. This observation indicates that the increase in cooperativity inferred from the dielectric spectra is not directly associated with the structural α–relaxation itself, but rather with intermediate-frequency collective motions of the hydrogen-bond network. Moreover, the structural relaxation observed in the Kerr effect signal displays a non-exponential character, which is well reproduced by a stretched exponential function, a behaviour that appears largely hidden in the dielectric response.

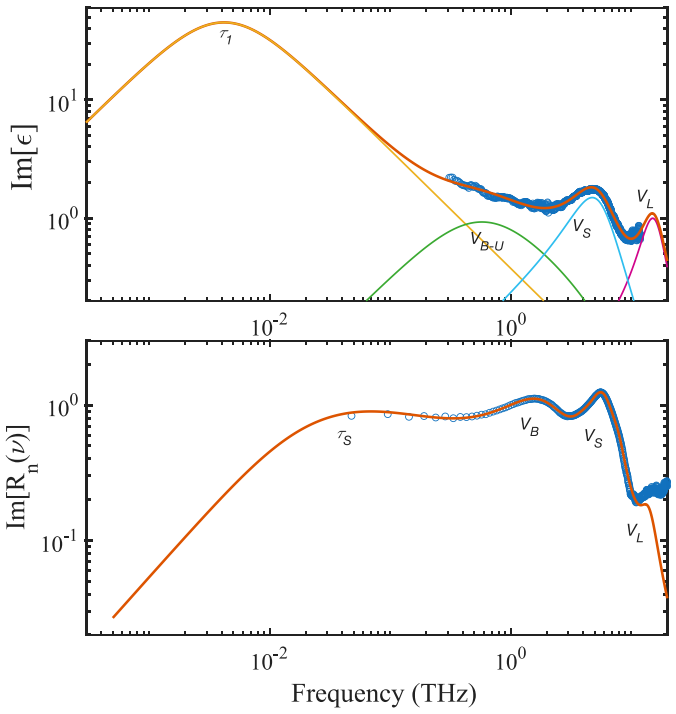

Fig. 9. Frequency behavior of the imaginary part of the complex dielectric constant of water at 255 K with the fitting curve obtained with model 2 (upper panel) and the third-order susceptibility at 253 K obtained from the Fourier transform of the optical Kerr effect signal [22,31] (lower panel) (τ_S denoting the structural α-relaxation and V_B the bending mode). The comparison clearly shows that, at low temperatures, the fast relaxation component of the dielectric response and the structural relaxation measured by depolarized Raman scattering may reflect different molecular dynamics, contrary to what might be inferred from a comparison at room temperature.

4. Conclusion

This study presents a comprehensive analysis of the optical properties of water using broadband Terahertz Time-Domain Spectroscopy (THz-TDS) over a wide frequency range (0.3–12 THz) and at various temperatures, extending into the supercooled phase. Using two distinct THz-TDS setups, we measured the absorption coefficient and refractive index of water with high precision. These two systems enabled broadband spectral measurements performed both in transmission and in attenuated total reflection (ATR) modes. The results obtained from the two techniques show excellent consistency and significant spectral overlap.

The dielectric response of water in the low-THz region is often described by introducing a secondary Debye relaxation to account for the high-frequency excess (the so-called “Debye wing”). However, such a phenomenological decomposition does not uniquely identify distinct molecular populations and may lead to ambiguous interpretations. In the present work, broadband dielectric spectra with high signal-to-noise ratio allow us to track the evolution of the spectral weight across different dynamical contributions. Two fitting approaches (two Debye plus two oscillators and one Debye plus three damped harmonic oscillators) consistently indicate a progressive redistribution of the response upon cooling: the contribution associated with librational (local rotational) motion decreases, while the intermediate-frequency component, often modeled as a second Debye term, gains spectral weight. This behaviour points to a gradual transition from predominantly local molecular dynamics at high temperature to increasingly collective dynamics at lower temperature. This is further supported by the transition from an almost critical vibrational character to an overdamped relaxational regime of the bending-umbrella mode in the second model. In this framework, the intermediate-frequency response is interpreted as a manifestation of the vibrational dynamics of the hydrogen-bond network. This interpretation is consistent with the picture proposed by Gaiduk, where the high-frequency wing originates from coupled bending–stretching fluctuations of hydrogen bonds, and with the model of Popov, in which deviations from Debye behavior arise from collective fluctuations of the same hydrogen-bond network responsible for the primary relaxation. Therefore, the apparent second Debye contribution can be understood as a convenient parametrization of a continuous spectrum of correlated hydrogen-bond network dynamics. The observed temperature dependence reflects an increasing cooperativity of the hydrogen-bond network, rather than the emergence of a distinct molecular relaxational channel. This scenario is compatible with a progressively larger contribution of LDL-like local environments, characterized by a more tetrahedral hydrogen-bond network and enhanced dynamical correlations.

Finally, a comparison between the dielectric loss spectra and depolarized Raman susceptibility at lower temperatures clearly reveals the spectral separation between the fast relaxation process and the structural relaxation dynamics in water, a distinction particularly evident in the supercooled regime. This separation suggests that the Debye wing cannot be directly identified with the structural α-relaxation itself.

CRediT authorship contribution statement

A. Taschin: Writing – review & editing, Writing – original draft, Visualization, Validation, Supervision, Software, Methodology, Investigation, Formal analysis, Data curation, Conceptualization. **P. Bartolini:** Writing – review & editing, Software, Methodology, Investigation, Formal analysis, Data curation, Conceptualization. **L. Caminiti:** Writing – review & editing, Writing – original draft, Visualization, Validation, Formal analysis, Data curation. **A. Boschetti:** Writing – review & editing, Visualization, Validation. **S. Fanetti:** Writing – review & editing, Investigation. **R. Torre:** Writing – review & editing, Writing – original draft, Visualization, Validation, Supervision, Resources, Project administration, Methodology, Funding acquisition, Conceptualization.

Declaration of competing interest

The authors declare that they have no known competing financial interests or personal relationships that could have appeared to influence the work reported in this paper.

Acknowledgements

This research was funded by Next Generation EU Programme: I-PHOQS Infrastructure [IR0000016, ID D2B8D520, CUP B53C22001750006], Project CNR-FOE-LENS-2023, and European Union's Horizon Europe Research and Innovation Programme under the project APACE, Grant Agreement No. 101161312.

Appendix A. Supplementary data

Supplementary data to this article can be found online at doi:10.1016/j.molliq.2026.129935.

Data availability

Data will be made available on request.

References

[1] P. Debye, Polar Molecules, Chemical Catalog Co, New York, 1929.
[2] D.C. Elton, The origin of the debye relaxation in liquid water and fitting the high frequency excess response, Phys. Chem. Chem. Phys. 19 (2017) 18739–18749, https://doi.org/10.1039/C7CP02884A
[3] C. Rønne, S. Rud Keiding, Low frequency spectroscopy of liquid water using thz-time domain spectroscopy, J. Mol. Liq. 101 (1) (2002) 199–218. ISSN 0167-7322, https://doi.org/10.1016/S0167-7322(02)00093-4, https://www.sciencedirect.com/science/article/pii/S0167732202000934. Molecular Liquids. Water at the New Millenium.
[4] H. Yada, M. Nagai, K. Tanaka, Origin of the fast relaxation component of water and heavy water revealed by terahertz time-domain attenuated total reflection spectroscopy, Chem. Phys. Lett. 464 (4) (2008) 166–170. ISSN 0009-2614, https://doi.org/10.1016/j.cplett.2008.09.015, https://www.sciencedirect.com/science/article/pii/S0009261408012487.
[5] K. Shiraga, K. Tanaka, T. Arikawa, S. Saito, Y. Ogawa, Reconsideration of the relaxational and vibrational line shapes of liquid water based on ultrabroadband dielectric spectroscopy, Phys. Chem. Chem. Phys. 20 (2018) 26200–26209, https://doi.org/10.1039/C8CP04778B
[6] T. Wang, P. Klarskov, P.U. Jepsen, Ultrabroadband thz time-domain spectroscopy of a free-flowing water film, IEEE Trans. Terahertz Sci. Technol. 4 (4) (2014) 425–431, https://doi.org/10.1109/TTHZ.2014.2322757
[7] N.Q. Vinh, L.C. Doan, N.L.H. Hoang, J.R. Cui, B. Sindle, Correlation between macroscopic and microscopic relaxation dynamics of water: evidence for two liquid forms, J. Chem. Phys. 158 (20) (May 2023) 204507. ISSN 0021-9606, https://doi.org/10.1063/5.0142818
[8] C. Ronne, L. Thrane, P.-O. Astrand, A. Wallqvist, K.V. Mikkelsen, S.R. Keiding, Investigation of the temperature dependence of dielectric relaxation in liquid water by thz reflection spectroscopy and molecular dynamics simulation, J. Chem. Phys. 107 (14) (1997) 5319–5331, https://doi.org/10.1063/1.474242
[9] R. Buchner, J. Barthel, J. Stauber, The dielectric relaxation of water between 0°c and 35°c, Chem. Phys. Lett. 306 (1) (1999) 57–63. ISSN 0009-2614, https://doi.org/10.1016/S0009-2614(99)00455-8, https://www.sciencedirect.com/science/article/pii/S0009261499004558.
[10] A. Beneduci, Which is the effective time scale of the fast debye relaxation process in water? J. Mol. Liq. 138 (1) (2008) 55–60. ISSN 0167-7322, https://doi.org/10.1016/j.molliq.2007.07.003, https://www.sciencedirect.com/science/article/pii/S0167732207001316.
[11] I. Popov, P.B. Ishai, A. Khamzin, Y. Feldman, The mechanism of the dielectric relaxation in water, Phys. Chem. Chem. Phys. 18 (2016) 13941–13953, https://doi.org/10.1039/C6CP02195F
[12] J.K. Vij, D.R.J. Simpson, O.E. Panarina, Far infrared spectroscopy of water at different temperatures: ghz to thz dielectric spectroscopy of water, J. Mol. Liq. 112 (3) (2004) 125–135. ISSN 0167-7322, https://doi.org/10.1016/j.molliq.2003.12.014, https://www.sciencedirect.com/science/article/pii/S0167732203002915.
[13] T. Fukasawa, T. Sato, J. Watanabe, Y. Hama, W. Kunz, R. Buchner, Relation between dielectric and low-frequency Raman spectra of hydrogen-bond liquids, Phys. Rev. Lett. 95 (19) (Nov 2005) 197802.
[14] V.I. Gaiduk, J.K. Vij, The concept of two stochastic processes in liquid water and analytical theory of the complex permittivity in the wavenumber range 0-1000 cm-1, Phys. Chem. Chem. Phys. 3 (2001) 5173–5181, https://doi.org/10.1039/B106510F
[15] V.I. Gaiduk, B.M. Tseitlin, Molecular Models for Calculation of Dielectric/Far-Infrared Spectra of Liquid Water, vol. 2, John Wiley & Sons, Ltd, 2003, pp. 65–331. https://doi.org/10.1002/0471466603.ch2. ISBN 9780471466604. https://onlinelibrary.wiley.com/doi/abs/10.1002/0471466603.ch2.
[16] V.G. Artemov, A unified mechanism for ice and water electrical conductivity from direct current to terahertz, Phys. Chem. Chem. Phys. 21 (2019) 8067–8072, https://doi.org/10.1039/C9CP00257J
[17] A.A. Volkov, S.V. Chuchupal, Dielectric spectra of liquid water: ultrabroadband modeling and interpretation, J. Mol. Liq. 365 (2022) 120044. ISSN 0167-7322, https://doi.org/10.1016/j.molliq.2022.120044, https://www.sciencedirect.com/science/article/pii/S0167732222015823.
[18] P.H. Poole, F. Sciortino, U. Essmann, H.E. Stanley, Phase behaviour of metastable water, Nature 360 (1992) 324–328.
[19] C. Huang, K.T. Wikfeldt, T. Tokushima, D. Nordlund, Y. Harada, U. Bergmann, M. Niebuhr, T.M. Weiss, Y. Horikawa, M. Leetmaa, M.P. Ljungberg, O. Takahashi, A. Lenz, L. Ojamäe, A.P. Lyubartsev, S. Shin, L.G.M. Pettersson, A. Nilsson, The inhomogeneous structure of water at ambient conditions, PNAS 106 (2009) 15214–15218.
[20] P. Gallo, K. Arnann-Winkel, C.A. Angell, M.A. Anisimov, F. Caupin, C. Chakravarty, E. Lascaris, T. Loerting, A.Z. Panagiotopoulos, J. Russo, J.A. Sellberg, H.E. Stanley, H. Tanaka, C. Vega, L.M. Xu, L.G.M. Pettersson, Water: a tale of two liquids, Chem. Rev. 116 (13) (2016) 7463–7500. ISSN 0009-2665, https://doi.org/10.1021/acs.chemrev.5b00750. <Go to ISI>://WOS:000379794000002.
[21] K.H. Kim, A. Späh, H. Pathak, F. Perakis, D. Mariedahl, K. Amann-Winkel, J.A. Sellberg, J.H. Lee, S. Kim, J. Park, K.H. Nam, T. Katayama, A. Nilsson, Maxima in the thermodynamic response and correlation functions of deeply supercooled water, Science 358 (6370) (2017) 1589–1593. ISSN 0036-8075, https://doi.org/10.1126/science.aap8269, https://science.sciencemag.org/content/358/6370/1589.
[22] A. Taschin, P. Bartolini, R. Eramo, R. Righini, R. Torre, Evidence of two distinct local structures of water from ambient to supercooled conditions, Nat. Commun. 4 (Sep 2013) 2401. ISSN 2041-1723, https://doi.org/10.1038/ncomms3401, http://www.nature.com/doifinder/10.1038/ncomms3401.
[23] A. Nilsson, L.G.M. Pettersson, The structural origin of anomalous properties of liquid water, Nat. Commun. 6 (2015) 8998. ISSN 2041-1723, https://doi.org/10.1038/ncomms9998. <Go to ISI>://WOS:000367579100004.
[24] C. Yang, M. Ladd-Parada, K. Nam, S. Jeong, S. You, A. Spah, H. Pathak, T. Eklund, T.J. Lane, J.H. Lee, I. Eom, M. Kim, K. Amann-Winkel, F. Perakis, A. Nilsson, K.H. Kim, Melting domain size and recrystallization dynamics of ice revealed by time-resolved x-ray scattering, Nat. Commun. 14 (1) (2023) 3313. ISSN 2041-1723 (Electronic) 2041-1723 (Linking). https://doi.org/10.1038/s41467-023-38551-0, https://www.ncbi.nlm.nih.gov/pubmed/37316494.
[25] R. Torre, P. Bartolini, R. Righini, Structural relaxation in super-cooled water by time-resolved spectroscopy, Nature 428 (2004) 296–298, https://doi.org/10.1038/nature02409
[26] A. Taschin, P. Bartolini, J. Tasseva, R. Torre, Thz time-domain spectroscopic investigations of thin films, Measurement 118 (2018) 282–288. ISSN 0263-2241, https://doi.org/10.1016/j.measurement.2017.05.074, https://www.sciencedirect.com/science/article/pii/S0263224117303871.
[27] V.A. Andreeva, O.G. Kosareva, N.A. Panov, D.E. Shipilo, P.M. Solyankin, M.N. Esaulkov, P.G. de Alaiza Martínez, A.P. Shkurinov, V.A. Makarov, L. Bergé, S.L. Chin, Ultrabroad terahertz spectrum generation from an air-based filament plasma, Phys. Rev. Lett. 116 (Feb 2016) 063902, https://doi.org/10.1103/PhysRevLett.116.063902
[28] L. Bergé, K. Kaltenecker, S. Engelbrecht, A. Nguyen, S. Skupin, L. Merlat, B. Fischer, B. Zhou, I. Thiele, P.U. Jepsen, Terahertz spectroscopy from air plasmas created by two-color femtosecond laser pulses: the ALTESSE project, EPL (Europhys. Lett.) 126 (2) (Jun 2019) 24001, https://doi.org/10.1209/0295-5075/126/24001
[29] M. Heyden, J. Sun, S. Funkner, G. Mathias, H. Forbert, M. Havenith, D. Marx, Dissecting the thz spectrum of liquid water from first principles via correlations in time and space, Proc. Natl. Acad. Sci. 107 (27) (2010) 12068–12073, https://doi.org/10.1073/pnas.0914885107
[30] D. Sharma, B. Das, A. Chandra, Terahertz spectrum of water at varying temperatures from 260 to 340 k: contributions from permanent and induced dipole correlations at different length scales, J. Phys. Chem. B 127 (30) (2023) 6714–6725, https://doi.org/10.1021/acs.jpcb.3c03241. PMID: 37477243.
[31] A. Taschin, P. Bartolini, R. Eramo, R. Righini, R. Torre, Optical Kerr effect of liquid and supercooled water: the experimental and data analysis perspective, J. Chem. Phys. 141 (8) (Aug 2014) 084507. ISSN 0021-9606, https://doi.org/10.1063/1.4893557, http://scitation.aip.org/content/aip/journal/jcp/141/8/10.1063/1.4893557.
[32] W. Withayachumnankul, B.M. Fischer, D. Abbott, Material thickness optimization for transmission-mode terahertz time-domain spectroscopy, Opt. Express 16 (10) (May 2008) 7382–7396, https://doi.org/10.1364/OE.16.007382, https://opg.optica.org/oe/abstract.cfm?URI=oe-16-10-7382.

[33] D.L. MacFarlane, E.M. Dowling, Z-domain techniques in the analysis of fabry-perot étalons and multilayer structures, J. Opt. Soc. Am. A 11 (1) (Jan 1994) 236–245, https://doi.org/10.1364/JOSAA.11.000236, https://opg.optica.org/josaa/abstract.cfm?URI=josaa-11-1-236.

[34] A. Soltani, D. Jahn, L. Duschek, E. Castro-Camus, M. Koch, W. Withayachumnankul, Attenuated total reflection terahertz time-domain spectroscopy: uncertainty analysis and reduction scheme, IEEE Trans. Terahertz Sci. Technol. 6 (1) (2016) 32–39, https://doi.org/10.1109/TTHZ.2015.2505909

[35] P. Kužel, H. Němec, F. Kadlec, C. Kadlec, Gouy shift correction for highly accurate refractive index retrieval in time-domain terahertz spectroscopy, Opt. Express 18 (15) (Jul 2010) 15338–15348, https://doi.org/10.1364/OE.18.015338, https://opg.optica.org/oe/abstract.cfm?URI=oe-18-15-15338.

[36] P. Koleják, K. Postava, M. Mičica, P. Kužel, F. Kadlec, J. Pištora, Experimental gouy phase shift compensation in terahertz time-domain spectroscopy, Photonics Nanostructures – Fundam. Appl. 31 (2018) 129–133. ISSN 1569-4410, https://doi.org/10.1016/j.photonics.2018.06.011, https://www.sciencedirect.com/science/article/pii/S1569441017303048.

[37] F. Yang, L. Liu, M. Song, F. Han, L. Shen, H. Pengfei, F. Zhang, Uncertainty in terahertz time-domain spectroscopy measurement of liquids, J. Infrared Millim. Terahertz Waves 38 (2) (Feb 2017) 229–247.

[38] P. Koleják, K. Postava, M. Mičica, M. Vanwolleghem, J. Pištora, The gouy phase shift in terahertz time-domain spectroscopy and its experimental estimation, modelling and compensation, in: 2019 44th International Conference on Infrared, Millimeter, and Terahertz Waves (IRMMW-THz), 2019, pp. 1–2, https://doi.org/10.1109/IRMMW-THz.2019.8874240

[39] P. Madden, D. Kivelson, A Consistent Molecular Treatment of Dielectric Phenomena, John Wiley & Sons, Ltd, 1984, pp. 467–566. ISBN 9780470142806 https://onlinelibrary.wiley.com/doi/abs/10.1002/9780470142806.ch5.

[40] E.W. Castner, M. Maroncelli, Solvent dynamics derived from optical Kerr effect, dielectric dispersion, and time-resolved stokes shift measurements: an empirical comparison, J. Mol. Liq. 77 (1) (1998) 1–36. ISSN 0167-7322, https://doi.org/10.1016/S0167-7322(98)00066-X, https://www.sciencedirect.com/science/article/pii/S016773229800066X. Dielectric Friction and Molecular Relaxation in Dipolar Liquids.

[41] U. Kaatze, Complex permittivity of water as a function of frequency and temperature, J. Chem. Eng. Data 34 (4) (1989) 371–374, https://doi.org/10.1021/je00058a001

[42] C. Rønne, P.-O. Åstrand, S.R. Keiding, Thz spectroscopy of liquid H_2O and D_2O, Phys. Rev. Lett. 82 (Apr 1999) 2888–2891, https://doi.org/10.1103/PhysRevLett.82.2888

[43] C.G. Malmberg, A.A. Maryott, Dielectric constant of water from 0° to 100° c, J. Res. Natl. Bur. Stand. 56 (1) (1956) 1–8, https://doi.org/10.6028/jres.056.001

[44] D.P. Fernández, Y. Mulev, A.R.H. Goodwin, A database for the static dielectric constant of water and steam, J. Phys. Chem. Ref. Data 24 (1) (1995) 33–69, https://doi.org/10.1063/1.555977

[45] C.M. Bishop, Pattern Recognition and Machine Learning, Information Science and Statistics. Springer, New York, 2006. ISBN 978-0-387-31073-2.

[46] F. Kremer, A. Schönhals (Eds.), Broadband Dielectric Spectroscopy, Springer, Berlin, Heidelberg, 2003, https://doi.org/10.1007/978-3-642-56120-7. ISBN 978-3-642-56120-7.

[47] L. Xu, F. Mallamace, Z. Yan, F.W. Starr, S.V. Buldyrev, H.E. Stanley, Appearance of a fractional stokes–Einstein relation in water and a structural interpretation of its onset, Nat. Phys. 5 (8) (08 2009) 565–569, https://doi.org/10.1038/nphys1328

Supplemental Material for:

Broadband THz Time-Domain Spectroscopy of Water: Increasingly Cooperative Dynamics upon Cooling in the Debye-Wing Frequency Range

A. Taschin[1,2], P. Bartolini[2], A. Boschetti[2,3], L. Caminiti[2,4], S. Fanetti[2,5], and R. Torre[2,4*]

[1] *Consiglio Nazionale delle Ricerche - Istituto Nazionale di Ottica, CNR-INO, Via Nello Carrara 1, Sesto Fiorentino FI, 50019, Italy.*

[2] *European Lab. for Non-Linear Spectroscopy (LENS), Univ. di Firenze, via N. Carrara 1, I-50019 Sesto Fiorentino, Firenze, Italy.*

[3] *Instituto Nazionale di Ricerca Metrologica, Strade delle Cacce 91, I-10135 Torino, Italy.*

[4] *Dip. di Fisica e Astronomia, Univ. di Firenze, via G. Sansone 1, I-50019 Sesto Fiorentino, Firenze, Italy.*

[5] *Consiglio Nazionale delle Ricerche - Istituto di Chimica dei Composti OrganoMetallici, CNR-ICCOM, Via Madonna del Piano 10, I-50019 Sesto Fiorentino, Firenze, Italy.*

* corresponding author: taschin@lens.unifi.it

S1. EXPERIMENTAL DETAILS

A. Broadband THz-TDS experiment

The two color laser-induced air-plasma THz-TDS system employs high energy femtosecond pulses produced by a Ti:Sapphire Chirped-Pulse-Amplification (CPA) laser (Coherent Legend). Following Fig.S1, a 40 fs 3 mJ laser pulse with a wavelength of 800 nm and repetition rate of 1 KHz is divided in two parts, one for the THz pulse generation, the pump, an another one for the detection, the probe. The vertically polarized pump pulse passes thought a focusing lens (f = 200 mm) and after that into a 100 μm BBO crystal for the second harmonic (SH) generation. A dual-wavelength half-wave plate rotates the SH polarization allowing vertical parallel polarization for both the 800 nm and 400 nm pulses. These are together collinearly focused on air to produce an air plasma filamentation of some mm length. High power THz pulse (some μJ) is produced by different nonlinear phenomena, namely, four wave mixing, photo-ionization current, and plasma wave by ponderomotive force [1, 2]. Depending on the intensity level of the optical impulses involved, these effects can be more or less relevant and, generally, induce THz radiation at different frequency bands. Overall, the THz pulse generated has the spectral bandwidth equivalent to the optical bandwidth. Then, the THz pulse is guided into the sample and in the detection area by a traditional four parabolic mirrors THz-TDS configuration [3]. A 6 mm silicon plate after the first parabolic mirror removes all the residual optical radiation from the THz beam. The measurement of the THz field is based on the Air Biased Coherent Detection (ABCD) technique. The probe beam is focused by another lens (f = 300 mm) through a hole on the last parabolic mirror, which focalizes the terahertz beam. Thus, terahertz and optical beams, with parallel polarizations, are collinearly focused on air on a same spot to induce a second harmonic pulse by third order nonlinear response of the air. A pair of electrodes with a 1 mm gap, with 3 kV, 500 Hz ac bias, synchronized with the laser repetition rate, is placed across this spot. The 500 Hz oscillating electric field and the optical probe field, both parallel, produce a second harmonic signal by the same nonlinear phenomena on air. This SH signal constitutes the local field for the heterodyne detection of the second harmonic pulse generated by the THz pulse. Second harmonic radiation is then filtered by a 400 nm bandpass filter and sent into a photomultiplier tube, whose signal is measured by a lock-in amplifier referenced to the 500 Hz bias modulation frequency, its output is finally digitalized by an acquisition board. Time evolution of the THz pulse electric field is then obtained recording the output at changing of the time delay between the pump and probe pulses. A home-made software acquires the processed signal together with the reading of the delay line encoder retracing the final time dependent THz field. All the THz beam path is contained in a nitrogen purged chamber to reduce water vapor absorption.

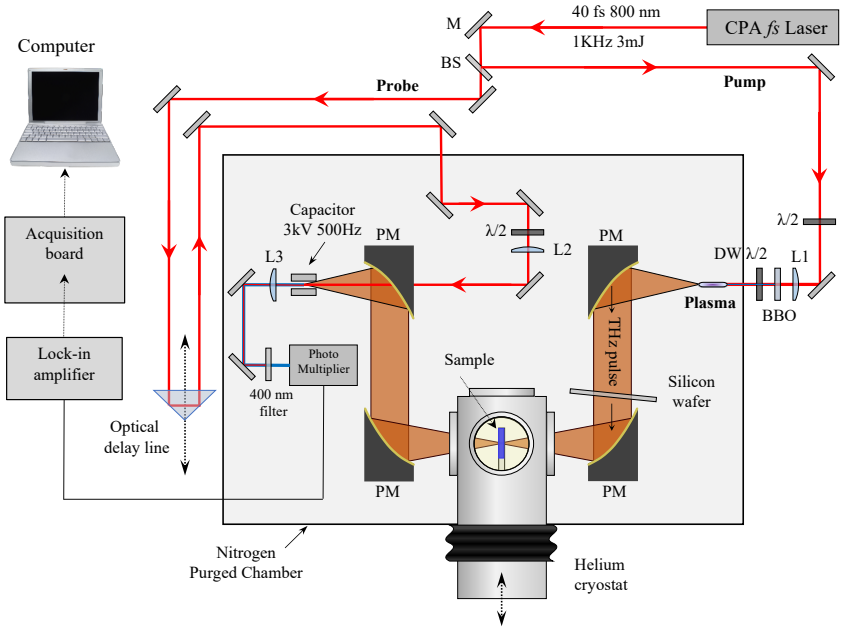

FIG. S1. Broadband THz-TDS setup with THz pulse generation by two colors laser-induced air-plasma and ABCD technique. The labeled elements are: M mirror, BS beam splitter, PM off axis parabolic mirror, L1-L3 lenses, BBO β-barium borate crystal, $\lambda/2$ half-wave plate, DW $\lambda/2$ dual-wavelength half-wave plate.

B. PCA THz-TDS experiment

PCA THz-TDS setup (see Fig.S2) uses a similar configuration for the THz beam guiding, with the only difference that THz emission and detection are obtained by two low-temperature-GaAs photoconductive antennas. THz pulses are produced by exciting the PCA with optical laser pulses with energy of around 1 nJ, at 780 nm, with pulse duration of 120 fs and a repetition rate of 100 MHz (produced by a T-light 780 nm fiber laser from MenloSystems). PCA is biased with sinusoidal voltage of 0-30 V at a frequency of 10 kHz. The antenna is coupled with a hemispherical silicon lens to extract the THz radiation from the chip more efficiently. The THz pulse after the sample is focused by an off-axis parabolic mirror on a identical PCA. Another hemispherical silicon lens optimizes the coupling between the THz field and the dipole of the detection antenna. The THz field, in this case, acts as a bias for the free carriers produced by a second optical pulse focused on the gap dipole. Electric field time evolution of the THz pulse is again obtained recording the photocurrent amplitude at varying of the time delay between the pump and probe pulses. Then the acquisition chain is very similar to that already described for the other setup. Even in this case, the whole THz set-up is enclosed in a nitrogen purged chamber.

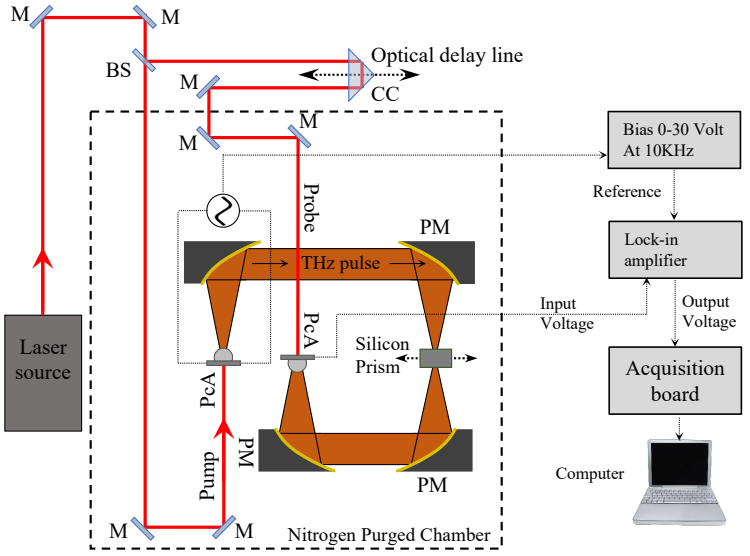

FIG. S2. PCA THz-TDS setup with THz pulse generation and detection by two photoconductive antennas. The labeled elements are: M mirror, BS beam splitter, PM off axis parabolic mirror, PcA photoconductive antenna.

C. Sample cells

The transmission measurements have been realized using a homemade cell (see Fig.S3) build with two circular diamond windows, 1 mm thick with diameter of 5 mm, and a 27 μm thick brass spacer washer with internal diameter of 3 mm. Two copper rings with six through screws closed and held the cell together. The cell was temperature controlled by a close cycle helium cryostat with a temperature stability of $\pm$ 0.1 K. The cell is filled with double distilled water. The thinness of the sample enable us extending the temperature range down to the supercooled region. Measurements were acquired in the range 255-360 K. Diamond is transparent to THz radiation as silicon, but it has the additional advantage to be transparent to the infrared or visible light giving access to spectroscopy experiments using mixed wavelength radiations.

The ATR measurements were done with a typical configuration using a 45° silicon prism. The home made cell for ATR measurements is shown in Fig.S4. The cell is constituted in the lower part by the surface of the silicon prism and in the remaining part by a Teflon septum with two chambers: one for containing the water sample for the water ATR signal and the other, left empty, for the reference measurement. Finally, an aluminum cap seals the cell. The whole cell holder was then temperature controlled by a thoermoelectric liquid chiller with a temperature stability of $\pm$ 0.1 K. We explored the temperature range 279-365 K. No measurements in the supercooled region were possible due to the instant crystallization of water in the ATR cell below the melting point temperature.

Water samples was taken from bi-distilled water sealed vials usually employed for pharmaceutical purpose.

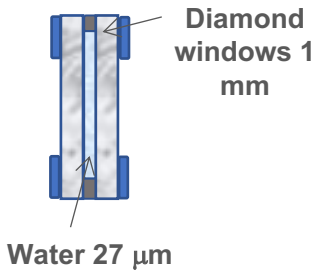

FIG. S3. Sample cell for transmission measurements: two circular diamond windows 1 mm thick and a 27 μm thick brass spacer washer in the middle are held together by two copper rings with six through screws. The cell is filled with double distilled water and temperature controlled by a close cycle helium cryostat with a temperature stability of $\pm$ 0.1 K.

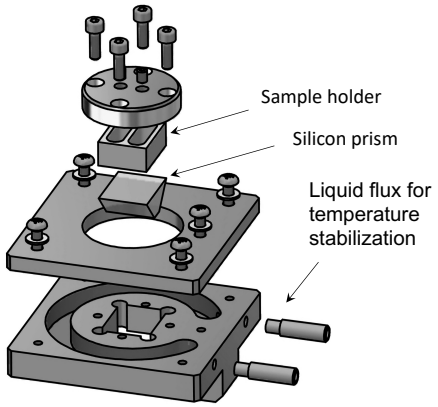

FIG. S4. Sample cell for ATR measurements. The cell is constituted in the lower part by the surface of the silicon prism and in the remaining part by a Teflon septum with two chambers, one for containing the water sample and the other, left empty, for the reference measurement. Finally, an aluminum cap seals the cell. The whole cell holder was temperature controlled by a thoermoelectric liquid chiller with a temperature stability of $\pm$ 0.1 K.

S2. MEASURED DATA

In Fig.S5 we show, in the upper panel, the typical time evolution of the THz electric field of the reference (blue line) and water cell signal (red line) obtained with the broadband THz setup at 255 K. Amplitude spectra of the reference and sample cell, obtained by Fourier transforms of the temporal signals, are shown in the lower panel. The dense regular oscillations visible across the water spectrum are due to internal reflections in the diamond windows. These reflections are not shown in the time evolution of the upper panel because they occur at times greater than 13 ps. This effect is, anyway, accounted for in the transfer function of the whole window-water-window system. The absorption peaks at around 8.4, 10.7 and 12.2 THz, more clearly visible in the reference spectra, are due to phononic resonances of silicon wafer used to block the pump beam. Fig.S6 shows in the upper panel the time evolution of THz electric field of reference (blue line) and water ATR signal (red line) measured by the PCA THz-TDS setup. Amplitude spectra of the reference and water temporal signals, obtained by their Fourier transforms, are shown in the lower panel. In both experimental setups, the sample cells are placed on a motorized translation stage to allow insertion and extraction of the cells into the THz beam. A reference measurement is taken for each single sample measurement. This reduces the effects on signal differences between reference and sample that can be occur on very slow times, such as those due to the temperature fluctuations, which are not related to the sample optical properties.

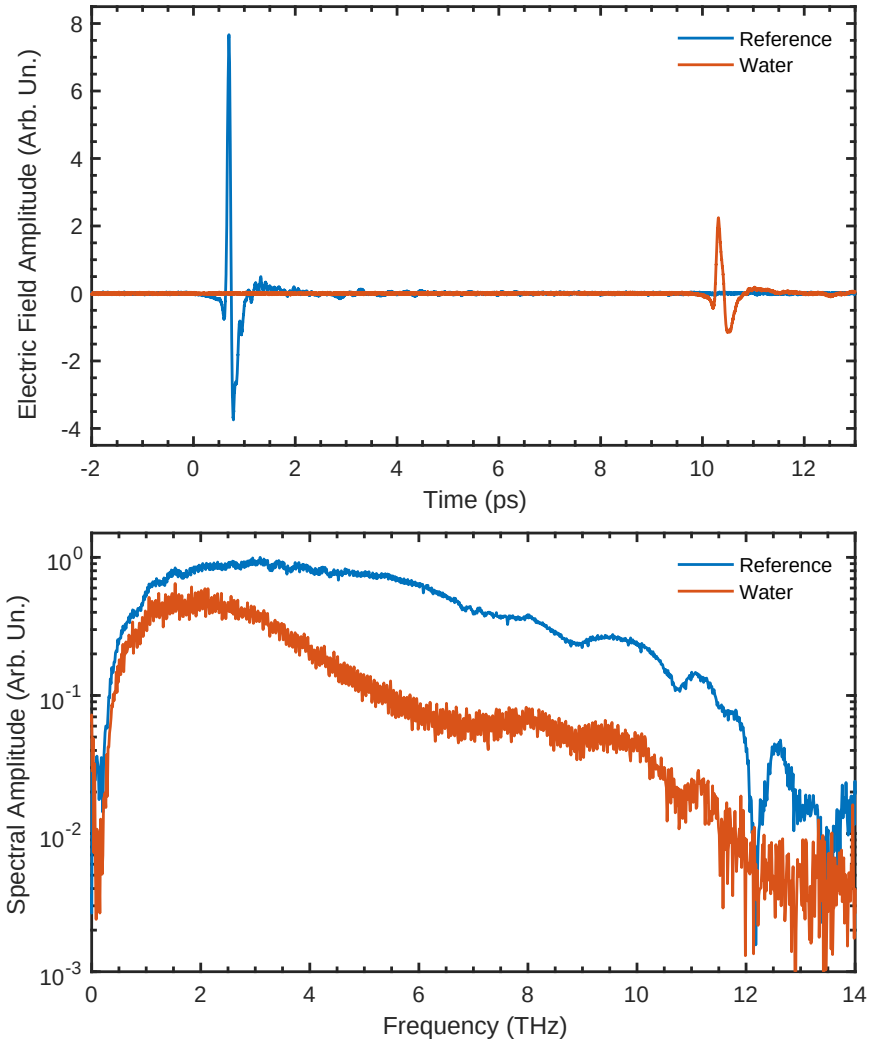

FIG. S5. Upper graph: time evolution of the THz electric field of the reference and water signal in transmission configuration with the broadband THz setup at 255 K, the delay accumulated by the sample pulse is mainly due to the diamond windows of the cell; lower graph: amplitude spectra obtained by Fourier transform of the signals on the top. The dense regular oscillations visible across the water spectrum are due to internal reflections in the diamond windows (in the upper graph these reflection pulses appear at times greater than 13 ps). This effect is accounted for in the transfer function of the whole window-water-window system. Absorption peaks at 8.4, 10.7 and 12.2 THz, more clearly visible in the reference spectra, are due to phonon resonances of silicon wafer.

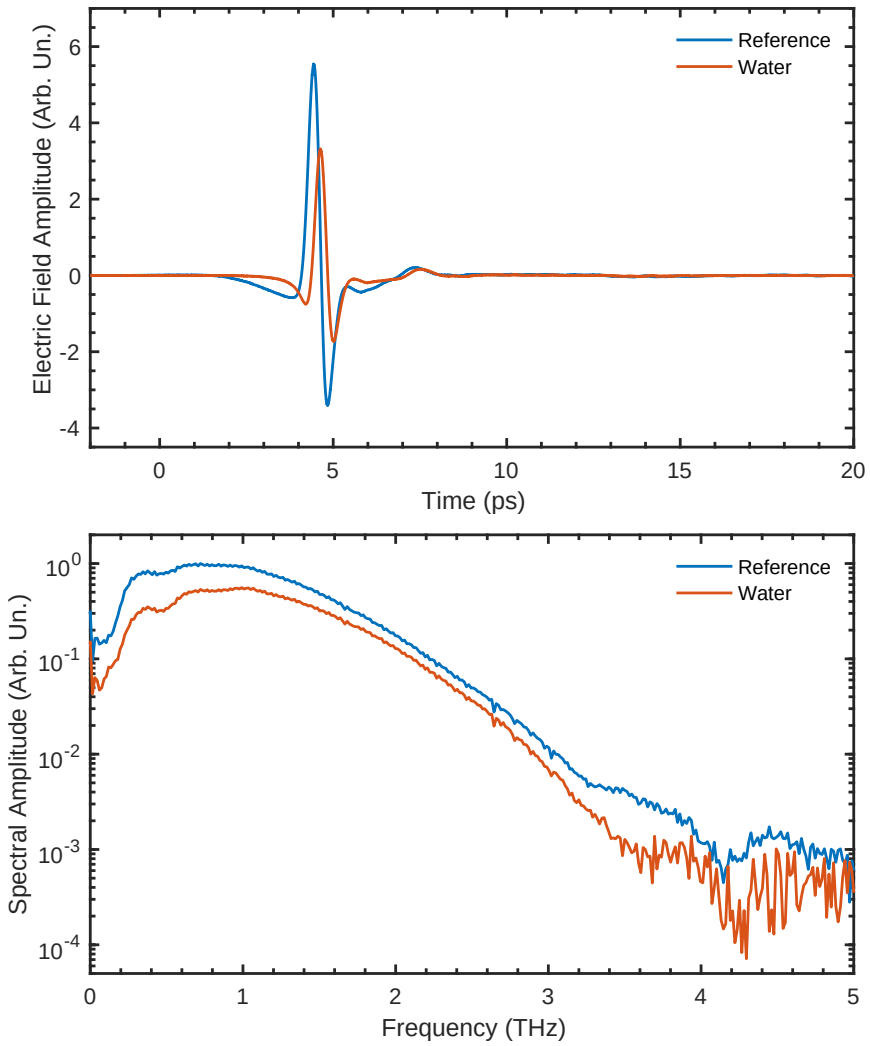

FIG. S6. Upper graph: time evolution of the THz electric field of the reference and water signal in ATR with the PCA THz setup at 298 K; lower graph: amplitude spectra obtained by Fourier transform of the signals on the top.

A. Coomparison with literature data

Our refractive index and water absorption coefficient values, $n(\omega)$ and $\alpha(\omega)$, were compared with the most important data reported in the literature. Some of these were obtained by Fourier-Transform Infra-Red (FTIR) spectroscopy measurements in ATR, reflection or transmission configuration. It is worth noting, that in these measurements the values of the refractive index are not directly measured but calculated from the values of the absorption coefficient through the Kramers-Kronig relations and this procedure relies on the complete knowledge of $\alpha(\omega)$ at all the frequencies. We would like to emphasize the importance of performing THz-TDS measurements for the simultaneous measurement of optical parameters. Other literature data are obtained by THz-TDS setups in ATR or reflection configuration only in a narrow THz range (0.1-2 THz). Only one paper report measurements in transmission configuration, on a free-standing film of water, with a broadband THz-TDS setup similar to ours [4]. In particular, we compare our results with those reported in the works of: Afsar and Hasted [5] that make FTIR measurements in reflection configuration, Thrane et *al.* [6] that use a THz-TDS experiment in reflection configuration, Zelsmann [7] that makes FTIR measurements in transmission configuration in a cell with a thin water sample, Rønne et *al.* [8] that make a THz-TDS in reflection configuration and finally Wang et *al.* [4] that performs a THz-TDS on a free standing water thin film in a broadband frequency range. Only in a few works the measurements were done as a function of temperature with more or less wide temperature ranges that only partially overlap our range, furthermore, for some studies, only measurements taken at a single temperature are reported. Thus we decide to compare the data at the

temperature T = 295 K at which Wang et al. [4] made the measurements (see Fig.S7). Our values and those of the literature for this temperature were obtained by interpolation when the temperature range allowed. When the measurements were done at only one temperature, we report the data without any manipulation as in the case of Afsar [5], Thrane et *al.* [6] and our ATR measurements with the Broadband THz-TDS setup.

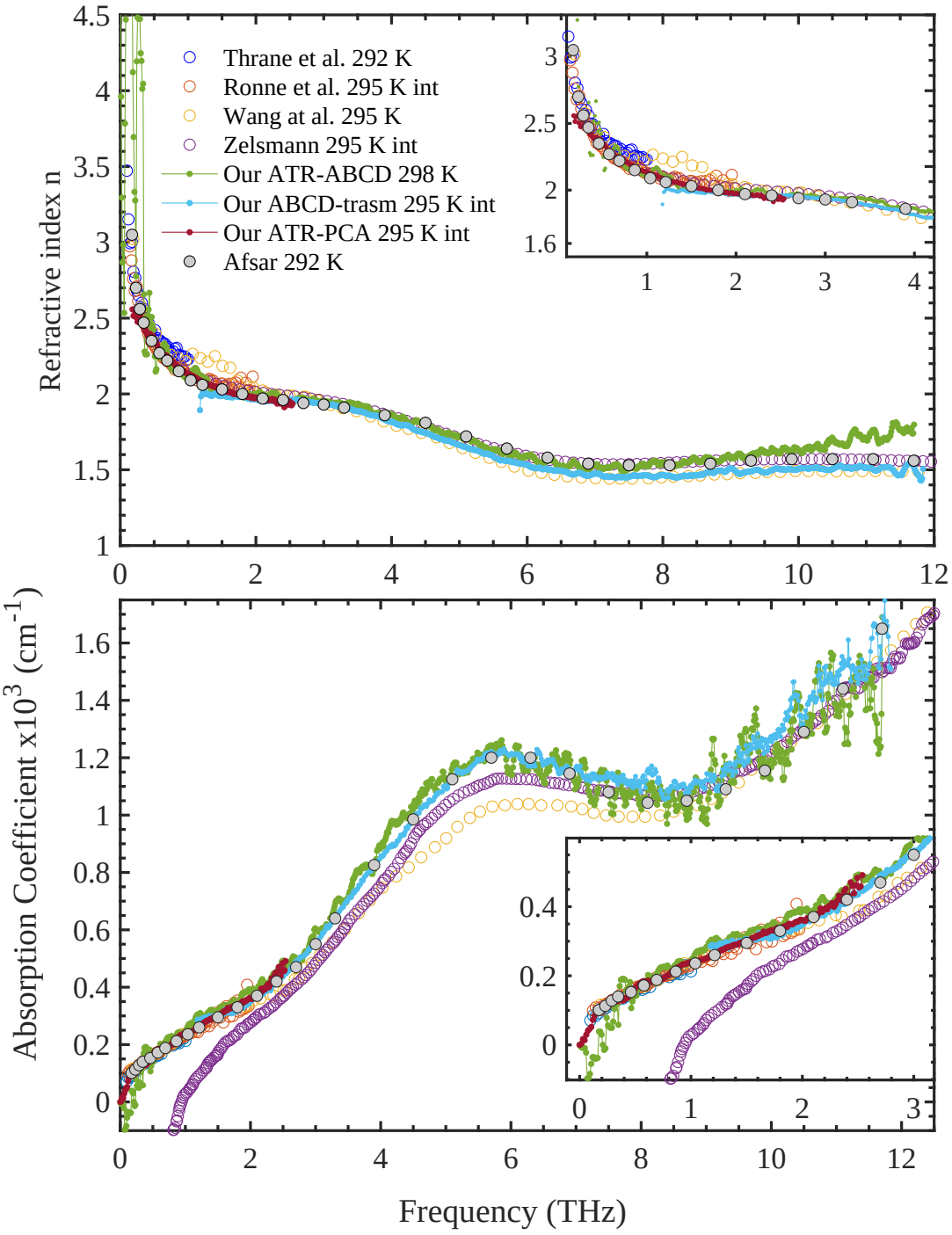

FIG. S7. Refractive index (upper panel) and absoption coefficient (lower panel) of water as function of frequency obtained from our measurements compared with the most important data reported in the literature [4–8]. The insets show the comparison in the low frequency range.

S3. DATA ANALYSIS

A. Fitting parameters

We report here the temperature dependence of the fixed fitting parameters obtained from literature and all the fitting parameters extracted from the data analysis with the two fitting models

T (K)	ε_S	τ_1 (ps)	ω_L (THz)
255	95.5300	38.0000	98.1273
260	93.3672	30.8125	97.4048
270	89.1875	20.3400	95.9596
280	85.1948	14.2000	94.5145
300	77.7377	8.1210	91.6242
320	70.9333	5.1865	88.7340
340	64.7245	3.5865	85.8437
360	59.0592	2.5550	82.9534

TABLE S1. Values of ϵ_S, τ_1 e ω_L used as fixed parameters in the fitting analysis and obtained respectively from [9], [10], and [11].

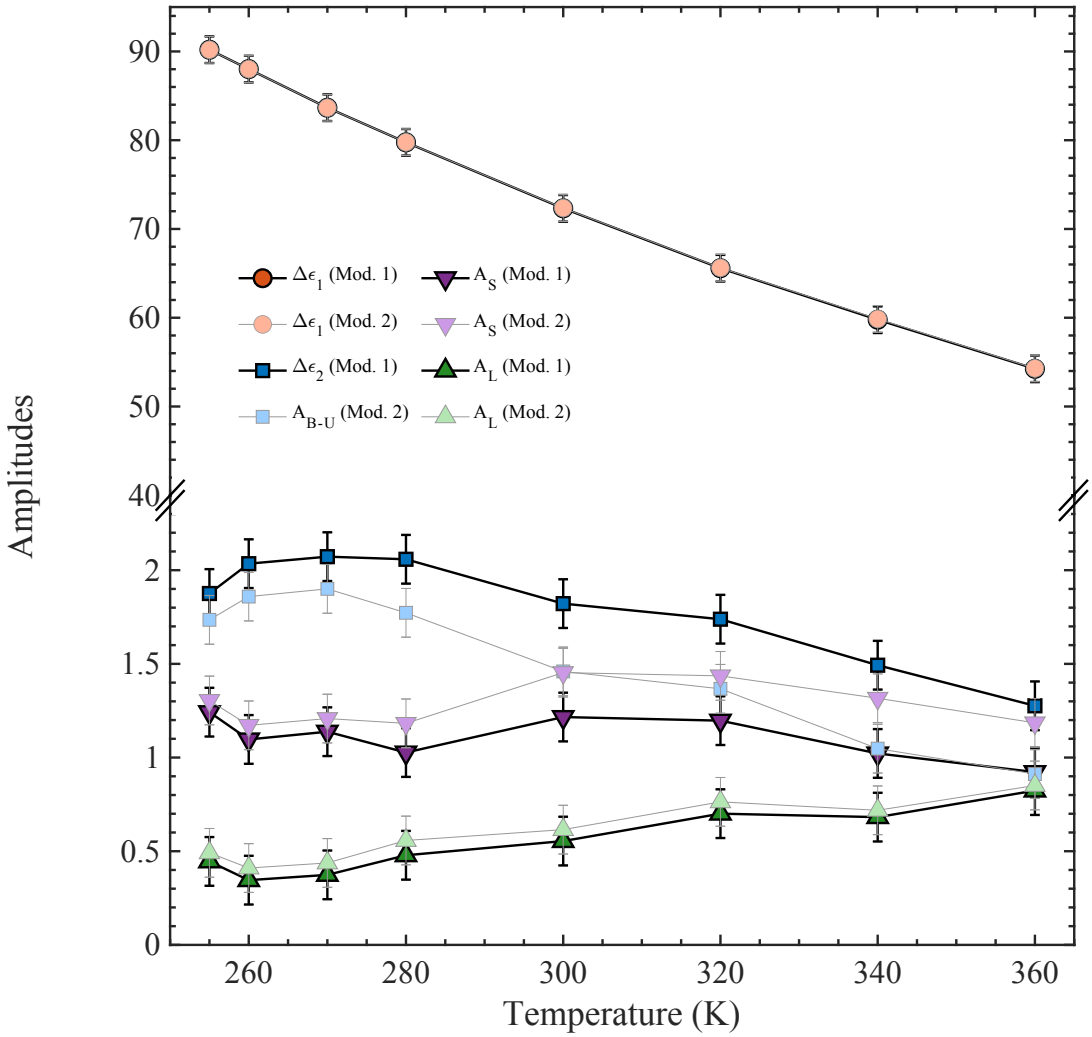

FIG. S8. Temperature dependence of the amplitudes associated with the different modes for both fitting models. Amplidute of the second Debye exists only for Model 1, and amplitude for bending-umbrella only for Model 2. Solid symbols for fitting Model 1, lighter symbols for fitting Model 2. The $\Delta\epsilon_1$ values obtained from the two models are nearly identical and overlap in the figure, so only one set of data points is visible.

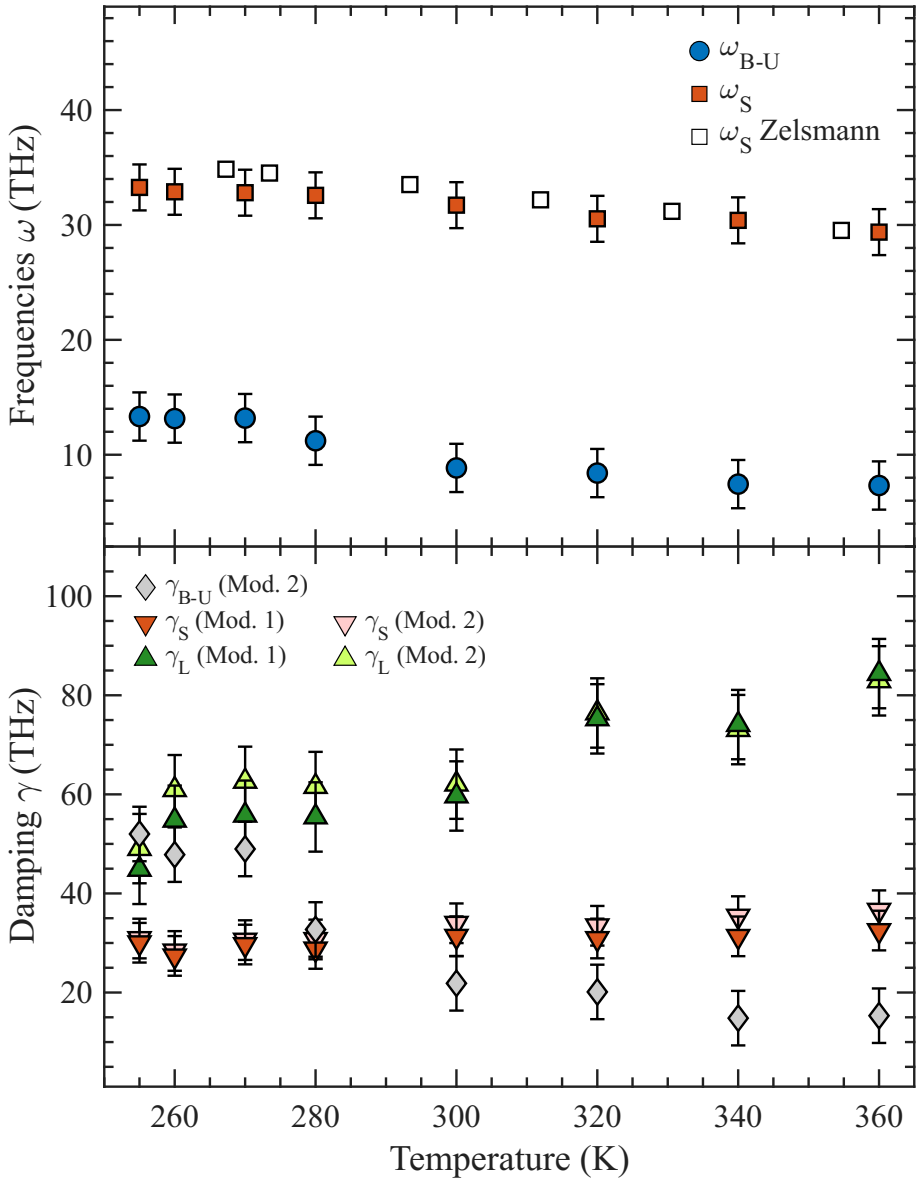

FIG. S9. Upper panel: Temperature dependence of the frequencies of the DHOs describing bending-umbrella, and stretching (the frequency values for the stretching DHO for the two model are practically identical). Stretching frequency values are in good agreement with those reported by [7]. Lower panel: damping constants of the DHOs describing bending-umbrella, stretching and librational modes in the two fitting applied models.

$\neq$

B. Implementation of the static-limit amplitude constraint

In the fitting procedure, the amplitudes of the different spectral contributions were constrained to satisfy the static dielectric limit. For both models used in the main text, the zero-frequency limit of the complex dielectric function can be written as

$$\varepsilon_S - \varepsilon_\infty = \sum_{i \in \mathcal{A}} A_i, \tag{S1}$$

where ε_S is the static dielectric constant, ε_∞ is the high-frequency electronic contribution, and $\mathcal{A}$ denotes the set of active spectral contributions in the chosen fitting model. The amplitudes A_i include the strengths of the Debye

relaxation terms and of the damped harmonic oscillator contributions, consistently with the definitions adopted in Eqs. (4) and (5) of the main text.

The condition in Eq. (S1) was not imposed by determining one amplitude as the residual difference between $\varepsilon_S - \varepsilon_\infty$ and the other fitted amplitudes. Instead, we used a normalized-weight parametrization. For each active component, an unconstrained fitting variable a_i was introduced and transformed into a positive normalized weight through a softmax transformation [12],

$$w_i = \frac{\exp(a_i)}{\sum_{j\in\mathcal{A}} \exp(a_j)}, \qquad i \in \mathcal{A}. \tag{S2}$$

Components not included in a given model were excluded from the normalization.

The physical amplitudes were then defined as

$$A_i = w_i \left(\varepsilon_S - \varepsilon_\infty\right), \qquad i \in \mathcal{A}. \tag{S3}$$

This parametrization automatically gives

$$\sum_{i\in\mathcal{A}} A_i = (\varepsilon_S - \varepsilon_\infty) \sum_{i\in\mathcal{A}} w_i = \varepsilon_S - \varepsilon_\infty, \tag{S4}$$

since $\sum_i w_i = 1$ by construction. Therefore, the static-limit condition fixes only the total dielectric strength, while the relative spectral weights of the active components remain adjustable fitting parameters.

For Model 1, the active amplitudes are

$$\mathcal{A}_1 = \{\Delta\varepsilon_1,\, \Delta\varepsilon_2,\, A_S,\, A_L\}, \tag{S5}$$

corresponding to the slow Debye relaxation, the fast Debye relaxation, the intermolecular stretching mode, and the librational mode. The bending–umbrella contribution is inactive in this model.

For Model 2, the active amplitudes are

$$\mathcal{A}_2 = \{\Delta\varepsilon_1,\, A_{B-U},\, A_S,\, A_L\}, \tag{S6}$$

corresponding to the slow Debye relaxation, the bending–umbrella mode, the intermolecular stretching mode, and the librational mode. The fast Debye contribution is inactive in this model.

This procedure has two practical advantages. First, it enforces the correct zero-frequency dielectric limit for each temperature. Second, it prevents unphysical negative amplitudes, since all weights w_i are positive by construction. Importantly, the constraint does not impose fixed relative weights among the intermediate-frequency and vibrational contributions; only their total static strength is normalized to $\varepsilon_S - \varepsilon_\infty$.

C. Sensitivity of the fitted amplitudes to the static constraint

To evaluate the possible influence of the static dielectric constraint on the extracted amplitudes, we repeated the fitting procedure by varying the input value of ε_S within a conservative range representative of the scatter among available literature data. In addition, we tested the influence of the high-frequency tail of the primary Debye relaxation by varying the fixed value of τ_1 within the uncertainty of the literature relaxation times.

Specifically, the fits were repeated using

$$\varepsilon_S^{\pm}(T) = \varepsilon_S(T)\left(1 \pm \delta_\varepsilon\right), \tag{S7}$$

and

$$\tau_1^{\pm}(T) = \tau_1(T)\left(1 \pm \delta_\tau\right), \tag{S8}$$

where δ_ε and δ_τ were chosen as conservative estimates of the uncertainty of the literature data, $\delta_\varepsilon = 0.01$ and $\delta_\tau = 0.02$.

The variations of ε_S mainly affect the absolute scale of the fitted amplitudes, as expected from Eq. (S3), since the total dielectric strength is proportional to $\varepsilon_S - \varepsilon_\infty$. However, the relative temperature evolution of the different spectral contributions is preserved. In particular, the intermediate-frequency contribution increases upon cooling, whereas the librational contribution decreases. The same qualitative behaviour is obtained when varying τ_1, showing

that the reported trends are not dominated by small uncertainties in the extrapolated high-frequency tail of the primary Debye relaxation.

The amplitudes ratios, $C_1(T)$ and $C_2(T)$ were also recomputed for all sensitivity tests. Their monotonic increase upon cooling is preserved within the tested uncertainty range (see Figure S10). This confirms that the main conclusion of the manuscript, namely the progressive enhancement of cooperative hydrogen-bond network dynamics upon cooling, does not arise from the specific implementation of the static-limit constraint.

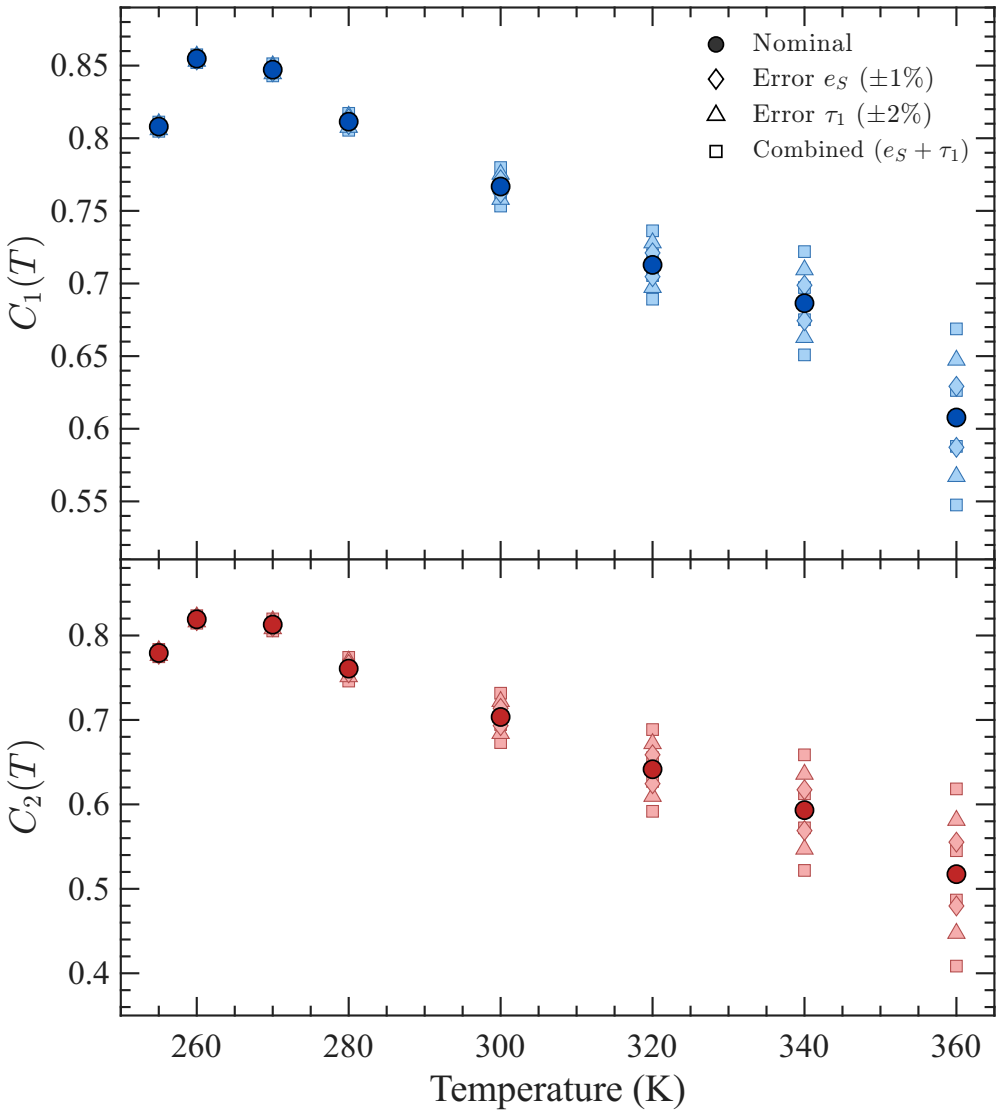

FIG. S10. Sensitivity of the normalized dielectric-strength ratios $C_1(T)$ (upper panel) and $C_2(T)$ (lower panel) to systematic variations of the fixed parameters ε_S and τ_1. Filled circles represent the nominal fits, while diamonds and triangles show the results obtained by varying ε_S by ±1% and τ_1 by ±2%, respectively. Squares indicate the results obtained when the two parameters are varied simultaneously within the same intervals. The overall temperature dependence of both ratios is preserved under all tested variations.

[1] V. A. Andreeva, O. G. Kosareva, N. A. Panov, D. E. Shipilo, P. M. Solyankin, M. N. Esaulkov, P. González de Alaiza Martínez, A. P. Shkurinov, V. A. Makarov, L. Bergé, and S. L. Chin, Phys. Rev. Lett. **116**, 063902 (2016).
[2] L. Bergé, K. Kaltenecker, S. Engelbrecht, A. Nguyen, S. Skupin, L. Merlat, B. Fischer, B. Zhou, I. Thiele, and P. U. Jepsen, EPL (Europhysics Letters) **126**, 24001 (2019).
[3] A. Taschin, P. Bartolini, J. Tasseva, and R. Torre, Measurement **118**, 282 (2018).

[4] T. Wang, P. Klarskov, and P. U. Jepsen, IEEE Transactions on Terahertz Science and Technology **4**, 425 (2014).
[5] M. N. Afsar and J. B. Hasted, J. Opt. Soc. Am. **67**, 902 (1977).
[6] L. Thrane, R. H. Jacobsen, P. U. Jepsen, and S. R. Keiding, Chemical Physics Letters **240**, 330 (1995).
[7] H. R. Zelsmann, Journal of Molecular Structure **350**, 95 (1995).
[8] C. Ronne, L. Thrane, P.-O. Astrand, A. Wallqvist, K. V. Mikkelsen, and S. R. Keiding, The Journal of Chemical Physics **107**, 5319 (1997), https://doi.org/10.1063/1.474242.
[9] G. A. Vidulich, D. F. Evans, and R. L. Kay, The Journal of Physical Chemistry **71**, 656 (1967), https://doi.org/10.1021/j100862a028.
[10] N. Q. Vinh, L. C. Doan, N. L. H. Hoang, J. R. Cui, and B. Sindle, The Journal of Chemical Physics **158**, 204507 (2023).
[11] H. Yada, M. Nagai, and K. Tanaka, Chemical Physics Letters **464**, 166 (2008).
[12] C. M. Bishop, *Pattern Recognition and Machine Learning*, Information Science and Statistics (Springer, New York, 2006).